

Magnetic Soft Actuator Design for Applications in Haptics

Submitted in partial fulfillment of the requirements for
the degree of
Doctor of Philosophy
in
Mechanical Engineering

Sarah Costrell

B.A. Mathematics, Brandeis University
M.A. Mathematics, Wake Forest University
M.S. Electrical Engineering, Boston University

Carnegie Mellon University
Pittsburgh, PA

December 2025

© Sarah Costrell, 2025
All Rights Reserved

Keywords: Haptics, Soft Robotics, Soft Materials

For my mom, Rickey – may her memory be a blessing.

Acknowledgments

This work was supported by several funding sources, including the Intelligent Symbiotic Systems Moonshot at Carnegie Mellon University and NSF Award 2312153: “Unboxing” Haptic Texture Perception: Closing the Loop from Skin Contact Mechanics to Novel Haptic Device. The work was supervised by my committee: Melisa Orta Martinez, Roberta L. Klatzky, Wui Yarn Daphne Chan, and Carmel Majidi.

I would like to thank all of my committee members for their mentorship throughout this process, especially Melisa and Bobby, who have spent countless hours helping me put together the research questions and approaches that form the basis of this thesis, and countless more in teaching me the intangibles of what it means to be an academic. I would not be the researcher I am today without everything I have learned from you. I would also like to thank all of the friends, colleagues, and collaborators here at Carnegie Mellon who have supported me in so many different ways; a woefully incomplete list of these individuals includes: Sam Speer, Abena Boadi-Agyemang, Kate Shih, Nataliya Rokhmanova, Bart Duisterhof, Chase Noren, Iqui Balam, Saul Schaffer, Taryn Immamura, Tito Babatunde, Mitch Fogelson, Jace Rozsa, Sunny Suprenant, Andrew Ashmar, Connor Valentine, and so many others. In developing and fabricating the polymers discussed in this work, I owe a great deal to the hard work and creative problem solving of the undergraduate researchers who have assisted me throughout my time here, and in particular I would like to thank Alex Zhao and Mahirah Alam, both of whom have been a source of pride and inspiration to me and who have given me a greater appreciation for the power of collaboration in scientific endeavors.

I am very lucky to have so many amazing individuals in my extended support network, without whom I never could have made it to this point. These include friends from undergrad and from the “sisterhood” of folks in my cohort of the Smith College Women in Math program, as well as all of the members of my family who have supported me along the way. I thank my cats, Thisbe and Hilbert, for loving me even though they cannot understand what “lab” is and why I need to leave them to go there. And of course, I thank my husband, Avik, whose compassionate nature and incredible dedication to all aspects of his life continue to inspire me every day; I am forever grateful for every homemade vegan cookie and every impromptu dance session, all of which have been vital in helping me finish out this Ph.D. journey.

Abstract

The sense of touch is an essential component of human perception and interaction with the environment. In order to replicate touch in virtual and remote systems, haptic engineers seek to develop devices that render tactile feedback through skin actuation. This thesis investigates a magnetic approach to haptic actuation through the development of wearable and externally driven soft magnetic devices. Specifically, we present the design, fabrication, and evaluation of magnetically responsive oleogel composites and their integration into fingertip-based haptic systems capable of rendering controllable tactile sensations. The first device, a fingertip-focused haptic actuator, combines a wearable composite sheath fabricated from a block copolymer (BCP) oleogel loaded with magnetic particles and an external electromagnet equipped with a field-focusing pole piece. Characterization experiments demonstrate that the composite material exhibits greater magnetic force transmission than conventional silicone elastomers under equivalent conditions. User studies of this device showed that perceived intensity scales linearly with electromagnet voltage and that attraction and repulsion modes produce indistinguishable perceptual responses, informing further stimulus design using this actuation method. Building on this foundation, we introduce MAGTRACE (Magnetic Texture Rendering for Active Contact and Exploration), a platform using dual electromagnets mounted on a linear rail to render spatially varying magnetic forces corresponding to virtual surface textures. Results from user studies indicate that participants were able to differentiate between waveform shapes and sizes at accuracies exceeding 80%, validating the efficacy of this actuation modality for macroscale texture rendering. Finally, we characterize the polymer composites underlying these devices, including SEBS/SEEPS triblock copolymer blends and Nd-Pr-Fe-B particle-filled magnetic elastomers. Through tensile, rheological, and magnetic deflection testing, we study the properties of BCP oleogels and establish a library of low-modulus formulations ($\approx 1\text{--}80$ kPa) suitable for soft actuation. Taken together, this work contributes to the fields of haptics and soft robotics through the introduction of novel soft systems and design paradigms for magnetic elastomer-based tactile interfaces, and provides a framework for future work in conformable, shape-programmable soft actuation systems.

Contents

1	Introduction	1
2	Background and Related Work	3
2.1	Texture Rendering Approaches in Haptics	3
2.2	Magnetic Materials for Haptic Actuation	3
3	Development of a Magnetic Device for Fingertip-Focused Haptic Actuation	5
3.1	Device Description	5
3.2	Design and Characterization	6
3.2.1	External Electromagnetic Field Source	6
3.2.2	Wearable Fingertip Sheath	8
3.3	Psychophysical Validation	14
3.3.1	Experiment: User Perception of Sensation Intensity	14
3.3.2	Method	14
3.3.3	Results and Interpretation	15
3.4	Conclusions	16
4	MAGTRACE: An Electromagnetic Texture Rendering Platform	17
4.1	Device Overview	17
4.2	Design and Characterization	19
4.2.1	Wearable Magnetic Fingertip Sheath	19
4.2.2	Electromagnetic Actuation	20
4.2.3	Linear Rail and Sliding Exploration Platform	21
4.2.4	Spatial Rendering of Magnetic Force	21
4.2.5	Validation of Rendering	22
4.3	User Interaction Study	23
4.3.1	Stimulus Factors	24
4.3.2	Preliminary Exploratory Experiment	24
4.3.3	Main User Interaction Study	26
4.4	Conclusions	32
5	Characterization and Evaluation of Magnetic Oleogels for Haptics and Soft Robotics	33
5.1	SEBS/SEEPS Copolymer Blends	33
5.1.1	Tensile Testing	33

5.1.2	Development of a ‘Matching Silicone’	35
5.2	SEBS/SEEPS and Nd-Pr-Fe-B Composites	38
5.2.1	Deflection Testing	38
5.2.2	Modulus Testing	44
5.3	Conclusions	46
6	Conclusion	47
6.1	Thesis Contributions	47
6.2	Future Work	48
6.2.1	Further Composite Materials Experiments	48
6.2.2	Magnetic Elastomers for Conformable Gripping Systems	48
6.2.3	Shape-Programmable Interfaces	49
Bibliography		51

List of Figures

3.1	The fingertip actuation device, consisting of a wearable magnetic fingertip sheath and an external electromagnet.	6
3.2	Diagram of magnet with core, coil, and pole piece. The focal point of the magnetic field is dependent on θ , while the area and strength of the field are dependent on r_1 . The pole base radius r_2 is specified by the size of the electromagnet's core. The height of the pole piece h is defined by θ and r_1	7
3.3	Axial FEMM simulation of the flux density in and around the electromagnet with optimal pole piece height and coil current of 1 A.	8
3.4	Comparison of the predicted flux magnitude (FEMM simulation) vs. the experimentally measured flux magnitude 0.5 mm above the tip of the electromagnet pole piece. Error bars in the experimental data indicate the mean and standard deviation over 5 sets of measurements. Changing the direction of current results in the same field magnitude in the opposite direction.	9
3.5	The shear storage modulus G' of the oleogel composite material increases from approximately 2.5 kPa to 5.5 kPa under a magnetic field step input of 0.5 T. . . .	10
3.6	Left: Finger sheath mold including an inner dowel (orange) and the outer mold (yellow). Right: Mold and permanent magnet holder for inducing magnetic field in material.	11
3.7	Bidirectional behavior of the material due to the induced magnetic field. On the left, the material is attracted to the oppositely oriented magnetic field generated by the electromagnet. On the right, the direction of the field has changed and the material is now repulsed away from the electromagnet.	11
3.8	Force measurement model and experimental setup. (a) Force diagram (Equation 3.4) where k is the stiffness of the plunger and force sensor. The sensed force, F_s , is kx , where x is the vertical displacement of the simulated spring system due to the deflection of the composite material. (b) Experimental setup for measuring the attractive and repulsive forces generated by the material. When the electromagnet is powered, the material is either attracted or repulsed by the magnetic field. The material either pulls or pushes on the plunger, which transfers the force to the force sensor.	12

3.9	Force measurements for the attraction and repulsion of the selected material, the BCP oleogel made from Septon 4077 and Drakeol 34, versus the responses of Ecoflex 00-10, Ecoflex 00-30, Ecoflex 00-50, and Dragon Skin 30 with respect to the magnet. Error bars indicate the standard deviation of the data. (a) Force measurements under the attraction modality. (b) Force measurements under the repulsion modality.	13
3.10	Experiment setup: the finger of the user rests above a small opening the ground-ing dome while the electromagnet sits under the dome to provide actuation forces.	14
3.11	The average normalized magnitude estimate responses with standard errors. Both modalities, attraction and repulsion, exhibit linear relationships between voltage input and mean magnitude estimate.	15
4.1	MAGTRACE: A linear exploration platform for magnetic fingertip actuation us-ing dual electromagnets mounted on a low-friction sliding carriage. Here, the user holds their hand outside of the magnet apparatus, showing the magnetic fingertip sheath on their index finger.	18
4.2	Detailed view of the linear texture exploration platform, consisting of two center-focused electromagnets (held inside the yellow housing) mounted on a sliding carriage with a handle for the user to drive it bidirectionally across a linear rail as the magnets render virtual textures.	18
4.3	Detail of dual electromagnet setup, consisting of two identical electromagnets placed opposite to one another, with the finger sheath in between. The field di-rections of the electromagnets were chosen such that the bottom magnet repulses the sheath and the top magnet attracts it and the upward force on the sheath is maximized.	19
4.4	Force testing data demonstrating the response of an aluminum bending beam force sensor with magnetic sheath on the tip moving through the twelve stimuli defined by size and shape and rendered in user tests, as described in Sec. 4.2.5. The waveform shapes are generated by the PWM input described in Section 4.2.4.	22
4.5	Force testing setup consisting of a cantilever-style bending beam load cell with the magnetic fingertip sheath on the end. This experimental setup was used to capture the data in Fig. 4.4.	23
4.6	Iconographic depictions of nine texture stimuli presented to users in the GUI during the exploratory study. Each icon corresponds to a stimulus defined by size and shape, rendered by the device.	24
4.7	Individual confusion matrices for each of the eleven study participants. Columns are rendered stimulus environment; rows are responses. The color of each box represents the number of responses of that type. The matrices on the left side of the red line represent the higher-performing group (HPG) of subjects, while those on the right represent the lower-performing group (LPG). ST = sawtooth, SN = sine, SQ = square, and associated numbers are spacing in mm.	27
4.8	GUI for the main user interaction study, in which the user only had to pick from three icons during each trial, instead of nine icons as in the exploratory study.	28

4.9	Average total errors made at each size of spacing in the main user study. The number of overall errors were observed to decrease as the spacing size increased. Error bars represent the standard deviations of the data.	31
4.10	Average shape confusion errors for the 1 mm and 2 mm spacing conditions in the main user study. The majority of errors made at these sizes were between sine and square or sine and sawtooth.	31
5.1	Dogbone dimension standard for a Type IV sample from ASTM Standard D638-22: Standard Test Method for Tensile Properties of Plastics.	34
5.2	The total polymer weight percentage in a given sample vs. the elastic modulus of the sample. The remaining weight percentage in each formulation is made up of white mineral oil. The data regarding which grade of Septon comprised the majority of the polymer weight in each sample is also shown.	35
5.3	The changes in modulus observed as different grades of Septon are added to an oleogel formulation consisting of a constant weight percent of Septon 4033. . . .	36
5.4	Comparisons of the complex viscosity γ of three samples of an oleogel formulation made up of 5wt% Septon 4033 and three samples of a silicone formulation made up of Ecoflex 00-20 FAST and 80vol% silicone thinner during gelation and curing, respectively.	37
5.5	Comparisons of the shear storage and loss moduli (G' and G'') of three samples of an oleogel formulation made up of 5wt% Septon 4033 and three samples of a silicone formulation made up of Ecoflex 00-20 FAST and 80vol% silicone thinner during gelation and curing, respectively. In the right hand graph, the variation in initial G' between 06052025-3 and the other samples is likely due to the sample having begun to cure slightly earlier than the others.	37
5.6	Viscosity and modulus behavior during curing for Ecoflex 00-20 FAST with 30-50vol% silicone thinner. Terminal G' for this formulation is comparable to that of the tested oleogel.	41
5.7	Custom electromagnetic deflection testing setup for magnetic material. Top Left: Partial testing setup with fixed electromagnet. Top Right: Detail of clamped sample prior to deflection. Bottom: Full testing setup including clamped sample, electromagnet, and TM-X5000 Optical Measurement System.	42
5.8	Shear storage modulus G' behavior over time for variously prepared samples of 5wt% Septon 4033, 45wt% mineral oil, and 50wt% NdFeB particles. The samples were all exposed to an applied magnetic field of $B = 300$ mT for the majority of each experiment - the drops in modulus observed for samples 2 and 3 occurred after the field returned to 0 mT.	45
5.9	Impulse responses for variously prepared samples of 5wt% Septon 4033, 45wt% mineral oil, and 50wt% NdFeB particles with respect to a repeated 10 second step input of a 300 mT magnetic field.	46

List of Tables

3.1	Modulus data (without particles) and remanent field data (with particles) for different elastomers. All modulus data except for the oleogel data comes from the database associated with [43].	13
4.1	Two-factor (shape, spacing) confusion matrix presenting the aggregate data for the environment rendered by the device vs. the environment selected by the subject in the exploratory study. Variable key: ST2 ... ST6 : sawtooth wave 2mm ... 6mm, SN2 ... SN6 : sine wave 2mm ... 6mm, SQ2 ... SQ6 : square wave 2mm ... 6mm. Correct responses are highlighted in blue.	26
4.2	Post-study questionnaire results for the higher-performing group (HPG) and lower-performing group (LPG). Each prompt was answered with an integer between 1 (Strongly Disagree) and 7 (Strongly Agree).	27
4.3	Confusion matrix presenting the aggregate data for the first group of subjects in the main user study. Variable labels as in Fig. 4.7.	30
4.4	Confusion matrix for the aggregate data for the second group of subjects in the main user study.	30
4.5	The raw and adjusted averages of correct responses from the exploratory study and the main study. The confidence interval determined from the data indicates an improvement in identification accuracy between the exploratory and main studies.	32
5.1	Example of planned testing samples combining Septon 4033 and Septon 4077, with total BCP weight percentages from 5% to 30%.	34
5.2	Summary of results from SEBS/SEEPS combination sample fabrication and tensile testing, part I.	39
5.3	Summary of results from SEBS/SEEPS combination sample fabrication and tensile testing, part II.	40
5.4	Summary of initial deflection results regarding distance traveled and angle of material under attraction and repulsion.	43

Chapter 1

Introduction

The sense of touch is an integral part of the human experience, allowing us to interpret the material characteristics of our surroundings. In order to leverage touch in the context of human-computer interaction, haptic engineers have explored a variety of actuation approaches. For instance, to simulate contact with real-world environments, cutaneous force-based haptic devices render sensation through the deformation of the skin [21] via actuation based on various technologies such as pneumatics, hydraulics, and dielectric materials [33, 54].

As demand for improved VR and teleoperation technology increases, effective haptic texture rendering will be critical for creating immersive virtual environments. To that end, this proposal presents our work on developing and characterizing composite materials based on block copolymer (BCP) oleogels and neodymium alloy magnetic particles. Our contributions are as follows:

- **Chapter 3:** The initial exploration and design framework around development of a magnetic haptic fingertip device, including:
 - Material characterizations, specifically regarding modulus and force transmission, and comparisons of the performance of magnetic actuators produced using BCP oleogels with those fabricated using silicone elastomers (Section 3.2.2.1)
 - An electromagnet design informed by the use of an optimally angled pole piece in order to better focus the magnetic field (Section 3.2.1)
 - The testing of the BCP oleogel fingertip device together with the electromagnet on a set of human users, with results showing a linear relationship between the range of input voltages and perceptual magnitude and indicating that the device can be used to provide a range of sensations (Section 3.3)
- **Chapter 4:** The extension of the design of the paradigm from Chapter 3 for the purpose of macro-scale texture rendering, specifically including:
 - The design of MAGTRACE (MAGnetic Texture Rendering for Active Contact and Exploration), a platform using dual electromagnets to render sensations to the index finger of the user in an exploratory context; as users move the sliding carriage along the linear rail with their right hand, the electromagnetic forces on their extended,

sheath-wearing index finger increase or decrease depending on the location of the carriage along the linear rail in order to render a different portion of the macro-scale texture (Sections 4.1, 4.2)

- Experimental results indicating that MAGTRACE produces differentiable macro-scale texture environments, specifically that users were able to identify waveform shapes at a rate above 80% (Section 4.3.3)
- **Chapter 5:** Our characterization approach for BCP oleogels and magnetic composites, including:
 - A thorough sweep of sample fabrication and tensile testing on different combinations of triblock copolymers, resulting in a range (≈ 1 – 80 kPa) of low-modulus elastomers (Section 5.1)
 - The formulation of a matching silicone for the use of creating and testing magnetic composites with similar characteristics to those made with oleogels (Section 5.1.2)
 - A custom experimental setup and initial set of magnetic elastomer deflection testing measurements showing several compositions resulting in > 10 mm of total deflection under a focused magnetic field (Section 5.2.1)

Taken altogether, this thesis constitutes an interdisciplinary contribution to the area of soft haptic actuation. We seek to combine design paradigms motivated by a deep understanding of haptics and haptic experimentation with a well-informed approach to polymer fabrication and characterization, resulting in insights that will be of benefit to academic communities across the disciplines of haptics, soft robotics, chemical engineering, and materials science.

Chapter 2

Background and Related Work

2.1 Texture Rendering Approaches in Haptics

With emerging applications in virtual reality and teleoperation, haptic texture rendering has been an active area of research in both academia and industry for the past several decades [13, 14, 18, 20, 25, 31, 36, 65]. This research remains key for these applications due to the importance of the sense of touch in interpreting lived experiences, and because the integration of touch into virtual environments has the potential to make navigation of such spaces more natural for the user [9, 21, 22].

One particular modality of texture rendering involves direct stimulation of the skin as the fingertip moves through a virtual environment while in contact with a grounded tabletop platform [7, 54]. Researchers have pursued this rendering approach using various actuation methods, such as ultrasonic surface vibrations generated by piezoelectric actuators [11, 12, 49, 60, 63, 78] and friction modulation via electrostatic attraction [27, 28, 47]. Usually, these modalities involve a bare fingertip in direct contact with an explored material (e.g. glass), in which the material transmits friction or other sensations to the user. Approaches developed by [11, 48], in particular, involve the exploration of textures on a similar scale as those implemented in Chapter 4.

2.2 Magnetic Materials for Haptic Actuation

Magnetic elastomer composite actuators were first introduced in the form of cantilever-style deflecting beams [39] and have remained an active area of research due to their unique design advantages. They can be constructed without any onboard motors, pneumatic pumps, or other electronics, allowing them to be untethered and generally more lightweight than other types of actuators. In comparison with dielectric elastomers, the electromagnets required to drive the actuation for magnetic polymer composites use far lower voltage ranges (V vs. kV), making them easier and safer to use in human interaction environments [86].

Recently, magnetic elastomer composites have been used in the fabrication of soft robotic grippers [17, 26, 83, 84], robot locomotion [57, 61, 74], and micro-pumps for fluid injection [64]. As the technology advances, researchers have begun to incorporate magnetic actuation into tactile haptic devices. The FingerFlux system uses an array of electromagnets to provide directional force and vibration via a permanent magnet attached to the fingertip of a user [77]. Magnetips use an actuating coil to vibrate a magnet attached to the fingernail [46]. Other work has shown that an array of ferromagnetic discs embedded in a wearable fingertip device can provide lateral forces for detection of the edges of a fixed permanent magnet [72]. The MagnetIO system presents a similar but inverted design paradigm by attaching a voice-coil magnet to the fingernail and using it to actuate magnets located in grounded soft polymer patches [44]. Magnus [52] features linkage-mounted electromagnets situated near corresponding permanent magnets on each fingertip, using repulsive forces from the electromagnets to push the fingertips downward at varying frequencies.

In the last two decades, tabletop shape displays have employed ferrofluids, which are colloidal suspensions of nanoscale ferromagnetic particles, and magnetorheological materials, in which larger magnetic particles are dispersed in a viscous substrate [62], to provide tactile actuation. For both ferrofluids and magnetorheological materials, this actuation is due to a chaining phenomenon in which the particles chain together in the direction of the applied magnetic field, leading to anisotropic material properties with respect to the non-magnetized direction [45]. Early research involved pinch-grasp displays made from pouches filled with ferrofluid and actuated by one or more electromagnets [66]. A later device called the Mudpad featured a larger pouch stiffened at various points using a set of electromagnets beneath the pouch [35]. In recent work, these ferrofluid pouches are coupled with linearly-actuated permanent magnets that modulate the stiffness of the fluid by changing the distance between the magnets and the pouch [67]. In regard to magnetic elastomer composites, which are a subclass of magnetorheological materials, a Braille display has been developed using Ecoflex, a silicone rubber popular in soft robotics research, and magnetic nanoparticles [15].

In this thesis, we contribute to the body of work regarding magnetic haptic actuation via the devices discussed in Chapters 3 and 4. In Chapter 5, we discuss characterization approaches for the novel material with which we have fabricated our haptic devices.

Chapter 3

Development of a Magnetic Device for Fingertip-Focused Haptic Actuation

In this initial investigation, we introduced a novel haptic device composed of a wearable fingertip sheath, fabricated using an oleogel loaded with magnetic particles, and an external electromagnet. The sheath was actuated using the external magnetic field provided by the electromagnet, which was in turn equipped with a field-focusing pole piece. During the development of the device, we sought to select the oleogel composite best suited for the transfer of the magnetic force from the material to the skin in order to provide perceptible forces to the wearer. Here, we compare our composite to composites created with materials commonly used in the literature and find the force transfer from our material, as measured by a low-range force sensor, to be much greater when actuated under the same range of input voltages to the electromagnet. We also present a psychophysical user study that shows a linear relationship between this range of input voltages and perceptual magnitude. This result indicates that the device provides a range of tactile feedback that can be driven to a desired intensity of sensation through proportional voltage control.

3.1 Device Description

The device presented here (Fig. 3.1) consists of a wearable fingertip sheath fabricated from a composite material composed of an elastomer loaded with magnetic particles, together with an external electromagnet. The electromagnet generates a magnetic field, creating a force between the magnet and the particles in the material, which renders a perceptible force to the fingertip skin of the user. In previous psychophysics research, the threshold for fingertip force detection was established to be on the order of cN [38], and the force measurements reported in Section 4.2 meet that objective. As reported in Section 3.3, this device imparts supra-threshold forces such that perceptual intensity responds linearly to an increase in the voltage input to the electromagnet. In addition, bidirectional sensations can be generated as the material is pushed or pulled away from the skin by changing the polarity of the electromagnet.



Figure 3.1: The fingertip actuation device, consisting of a wearable magnetic fingertip sheath and an external electromagnet.

3.2 Design and Characterization

3.2.1 External Electromagnetic Field Source

The electromagnet was comprised of an iron pole piece, a ferrite (MnZn) pot core (TDK Electronics, B65684A0630A027), and a resin-printed printed bobbin (Formlabs Rigid 4000 Resin) to house the winding, which consisted of 1675 turns of 30 AWG copper magnet wire. We considered lower gauge wire in order to achieve greater current draw, but similar levels of magnetic field strength could be achieved by using a higher gauge and more coil turns. The selected core has a high initial relative permeability ($\mu_i = 2000$), which contributes to the concentration of the field within the core, and a field-shielding geometry.

The purpose of the iron pole piece on top of the core was to focus the magnetic field. Pole pieces concentrate the magnetic field at a pole over an area smaller than the base radius of the pole (r_2 in Fig. 3.2) [24]. While pole pieces often come in pairs in order to concentrate the field between them, single pole piece designs can also increase the axial flux density at the pole piece tip while decreasing the area over which the field is dispersed [50]. These characteristics boost magnetic field density at the desired stimulus location on the fingertip of the user. In the most general case [34], the magnetic field strength H at the focal point of a conical pole piece is

$$H = \frac{I_s}{2\mu_0} \sin^2 \theta \cos \theta \ln \frac{r_2}{r_1} \quad (3.1)$$

where I_s is the saturation magnetization of the material, μ_0 is the magnetic permeability of free space, θ is the angle between the hypotenuse of the pole piece and its focal point, r_1 is the radius

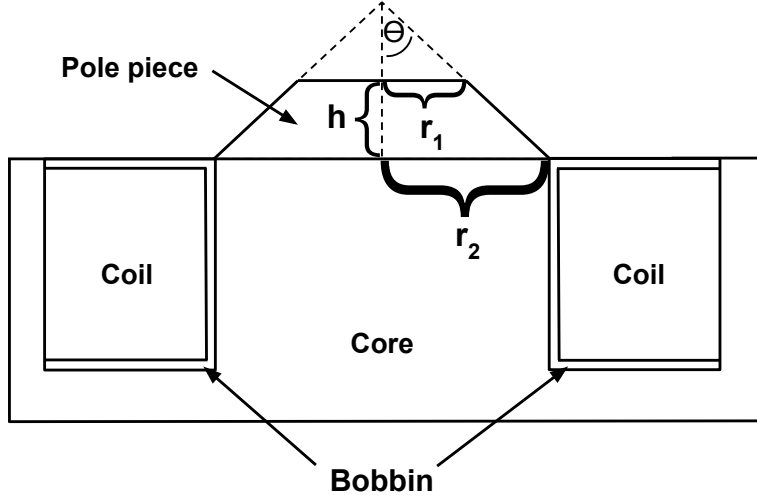


Figure 3.2: Diagram of magnet with core, coil, and pole piece. The focal point of the magnetic field is dependent on θ , while the area and strength of the field are dependent on r_1 . The pole base radius r_2 is specified by the size of the electromagnet's core. The height of the pole piece h is defined by θ and r_1 .

of the tip of the pole piece, and r_2 is the radius of the base of the pole piece (Fig. 3.2). The field strength is maximized when $\theta = 54.7^\circ$. As the flux density B is proportional to H via the relation $B = \mu_0(H + M)$, a maximal H will increase the force on the material according to Equation 3.2.

We analyzed our particular device using the open-source finite element method magnetic computation tool FEMM [6] in conjunction with the MATLAB optimization toolbox in order to confirm the optimal pole piece design. The pole piece used in the device is made of custom-machined iron with $r_1 = 0.5$ mm, in order to minimize the area of flux concentration, and $r_2 = 12.75$ mm, in order to match the radius of the ferrite core. Using a current input of 1 A and multi-point-seeding of fmincon with a constraint tolerance of 10^{-15} , r_1 and r_2 were held constant while the height of the iron pole piece was varied, with the goal of maximizing the flux at the tip of the pole piece. A local maximum was found at $h = 8.67$ mm, resulting in a value of $\theta = 54.71^\circ$, consistent with the angle predicted in Equation 3.1. Fig. 3.3 shows that, outside of the core, the highest magnitude of field strength is observed at the tip of the pole piece.

To evaluate the validity of the FEMM model, we tested the flux density at the tip of the custom-machined pole piece using a Gaussmeter and probe (FW Bell 5180). Fig. 3.4 shows the divergence between the predicted value of the magnetic field at the tip of the pole piece (calculated at 0.5 mm above the tip in the FEMM simulation) and the measured magnetic field at that point on the electromagnet. The experimental results suggest that the finite element model is representative of the behavior of the electromagnet; the average difference between the predicted and experimental field is 12.6%. This is likely due to imperfections in the core and pole piece material, bobbin fabrication, as well as in the machining and coil-winding process, which reduce the output of the electromagnet compared to its modelled capability.

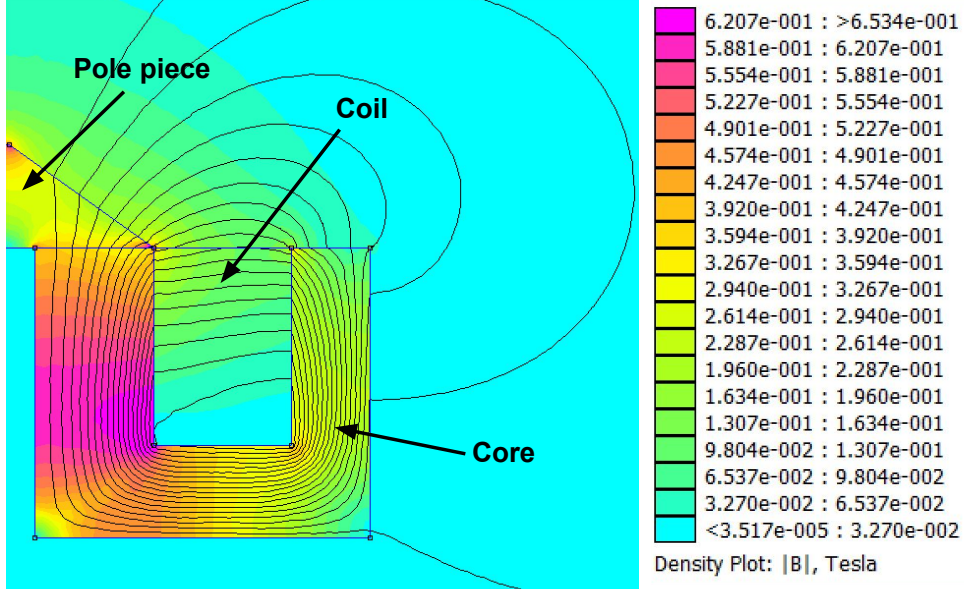


Figure 3.3: Axial FEMM simulation of the flux density in and around the electromagnet with optimal pole piece height and coil current of 1 A.

3.2.2 Wearable Fingertip Sheath

3.2.2.1 Material Choice

We designed the wearable component of the device to effectively transfer the force created by the magnetic field between the sheath and the external electromagnet to create perceptible tactile sensations. The force F_B generated by the interaction between the magnetic particles in the sheath and electromagnet is given by:

$$F_B = \nabla B \cdot M \quad (3.2)$$

where ∇B is the gradient of the flux density due to the electromagnet and M is the magnetization of the magnetic particles in the composite material [79]. To model the forces transferred from the material to the user, we can approximate the problem by considering a rectangular piece of material clamped at both ends and a point force applied at the midpoint between the clamped ends (Fig. 3.8a). In this case, the perpendicular deflection w of the material at the midpoint $x = \frac{L}{2}$ along the material is:

$$w = F_B \frac{L^3}{192EI} \quad (3.3)$$

where L is the length of the material between the clamps, F_B is the magnetic force approximated as a point force, E is the elastic modulus of the material, and I is the moment of inertia of the material [82]. Thus, when the dimensions and mass of the material are held constant, the deformation of the material is maximized when E is minimized. To measure the force transferred via the material, we can model a force sensor underneath the material as a spring in line with the

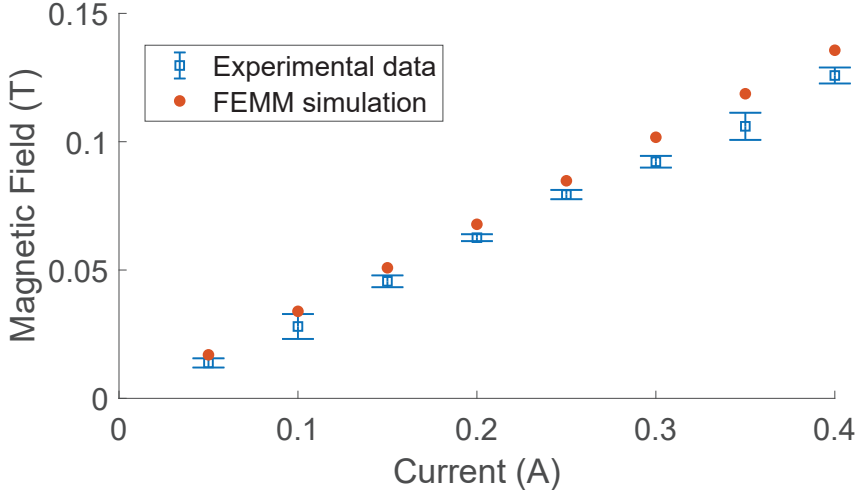


Figure 3.4: Comparison of the predicted flux magnitude (FEMM simulation) vs. the experimentally measured flux magnitude 0.5 mm above the tip of the electromagnet pole piece. Error bars in the experimental data indicate the mean and standard deviation over 5 sets of measurements. Changing the direction of current results in the same field magnitude in the opposite direction.

applied force F_B . In this case, the material will also be subjected to the reaction force from the spring, F_s , which is also equal to the measured force by the sensor:

$$F_s = F_B \frac{kL^3}{192EI + kL^3} \quad (3.4)$$

This model suggests that to maximize magnetic force transfer to the sensor, we would want near-zero stiffness in the substrate material. The modulus must, however, be high enough to provide sufficient yield stress in order to hold the magnetic particles in place. This simplistic model suggests we seek the most flexible material possible that is still able to retain the particle matrix in its fabricated arrangement and orientation. We acknowledge that this model is not a full representation of the contact between the material and human skin, as the skin constraints will be more compliant. The model does, however, provide an initial tool for material design. A higher-fidelity analysis of the interactions between the composite and the skin is a topic of future work.

Regarding material choice, the majority of soft robotics research involving magnetic composite materials utilizes silicone elastomers, such as polydimethylsiloxane (PDMS) [75]. The moduli of these elastomers ranges from tens of kilo to mega Pascals (kPa to MPa) due to their relatively high crosslinking density. While the density of PDMS can be varied by using different ratios of elastomer base to curing agent, the order of magnitude of the moduli remains constant [76]. A review of the moduli of the most commonly used silicone elastomers reports a range from 2.4 MPa, for Sylgard 184, to 0.05 MPa, for Ecoflex 00-10 [73]. For this application, in order to maximize F_s , we created a block copolymer (BCP) oleogel by combining a triblock copolymer commercially known as Septon 4077 (Kuraray America) with the mineral oil Drakeol 34 (Penreco). This oleogel is thermoreversible, meaning it is heated and then cooled for gela-

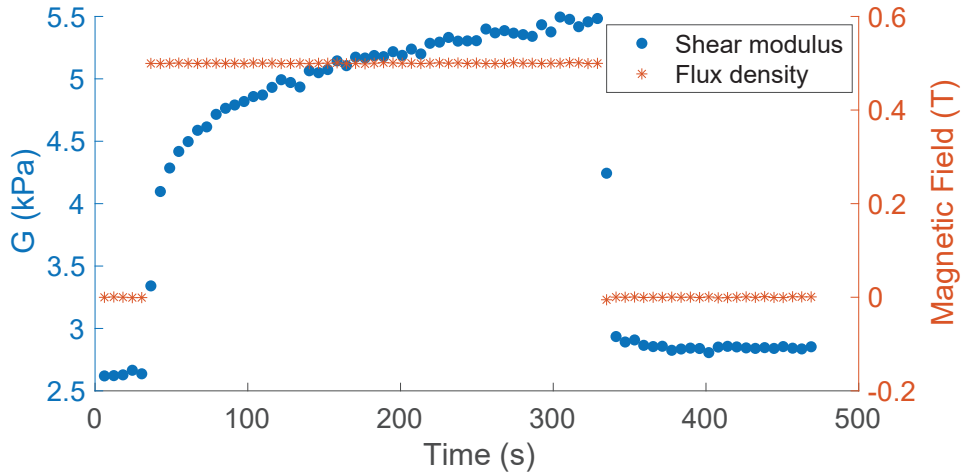


Figure 3.5: The shear storage modulus G' of the oleogel composite material increases from approximately 2.5 kPa to 5.5 kPa under a magnetic field step input of 0.5 T.

tion, as opposed to chemically crosslinked elastomers, so it can be reprocessed by reheating if the initial casting has any imperfections. The modulus of the BCP oleogel can be tuned using different proportions of oil and the triblock copolymer [16]. For the composite discussed in this work, we used a copolymer to oil ratio of 1:20 by mass.

The shear storage modulus G' for the BCP oleogel is ≈ 100 Pa in the low angular frequency range ($10^{-2} \leq \omega \leq 10^{-1}$), as measured using a frequency sweep procedure in the linear viscoelastic region for the material (strain = 1%) on a rheometer (DHR, TA Instruments). As $E = 2G(1 + \nu)$, where the Poisson ratio $\nu \approx 0.5$ for incompressible materials, the elastic modulus $E \approx 300$ Pa. As this value is several orders of magnitude lower than the reported moduli range for other commonly used elastomers [73], Equation 3.4 indicates that this elastomer can be expected to produce a greater transfer of force compared to soft materials generally used in haptic studies, such as Ecoflex and Dragon Skin [2, 70, 71, 85, 87]. When the material is combined with magnetic particles in a 1:1 ratio by weight, the modulus of the composite material increases. In Fig. 3.5, which shows measurements taken on a rheometer equipped with a magnetic testing accessory kit, the shear storage modulus of the composite material ranges from $\approx 2.5 - 5.5$ kPa, under an external magnetic field not exceeding 0.5 T. Since the magnetic field generated by the electromagnet used in this device does not exceed 0.5 T, the expected value of the modulus E is between 7.5 and 16.5 kPa during the operation of the device.

3.2.2.2 Material and Finger Sheath Fabrication

We constructed the fingertip sheath from a composite material made up of the BCP oleogel (1:20 Septon 4077 to Drakeol 34), loaded in a 1:1 ratio by weight with neodymium alloy (Nd-Pr-Fe-B) particles (Magnequench MQP-AA4-15-7, 150 mesh, flake geometry). These components are melt-mixed for 25 minutes at 210° C in a high-temperature-resistant resin mold (Fig. 3.6) and gelated by returning the material to room temperature. The mold for the sheath consists of an

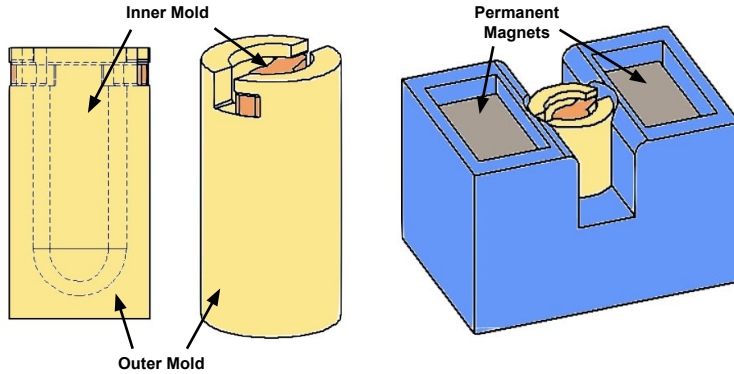


Figure 3.6: **Left:** Finger sheath mold including an inner dowel (orange) and the outer mold (yellow). **Right:** Mold and permanent magnet holder for inducing magnetic field in material.

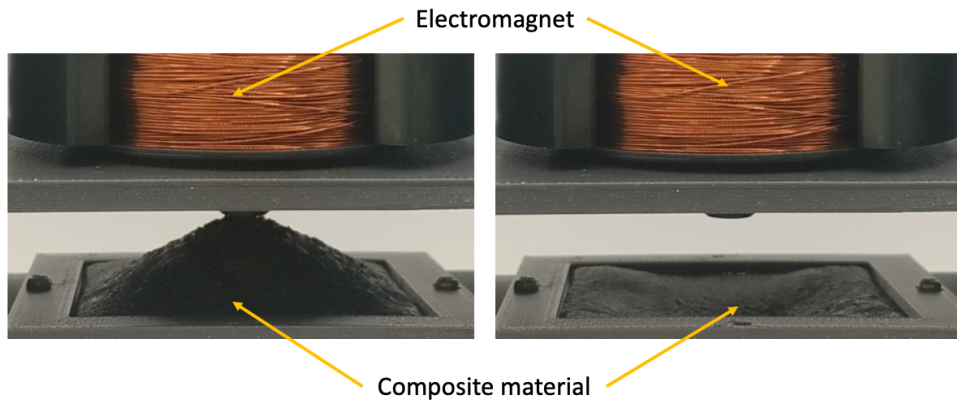


Figure 3.7: Bidirectional behavior of the material due to the induced magnetic field. On the left, the material is attracted to the oppositely oriented magnetic field generated by the electromagnet. On the right, the direction of the field has changed and the material is now repulsed away from the electromagnet.

inner dowel in the shape of a rounded-tip cylinder and an outer mold to create a 4 mm-thick sheath that stretches over the user's finger. The weight of the sheath was 8.45 g.

The magnetic particles have hard (permanent) magnetic properties, which we use to induce a magnetic field in the material. During gelation, we apply a 300 mT field from two permanent magnets, causing the dipoles within the particles to align themselves in the direction of this field. When the external field is removed, the induced magnetic field remains, leaving north/south poles within the material. This allows the material to be attracted by an opposite magnetic field or repulsed by a like magnetic field (Fig. 3.7).

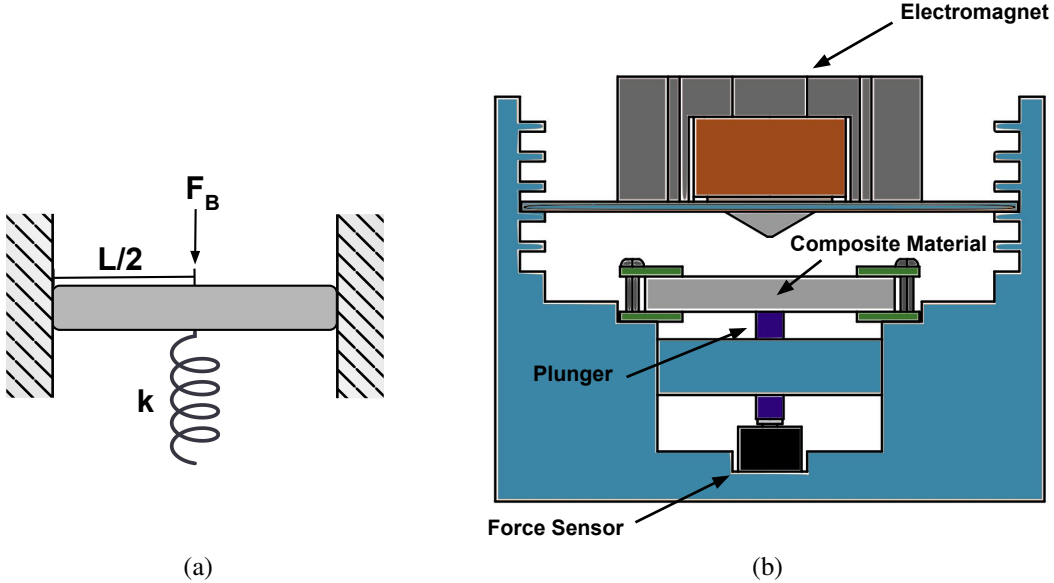


Figure 3.8: Force measurement model and experimental setup. (a) Force diagram (Equation 3.4) where k is the stiffness of the plunger and force sensor. The sensed force, F_s , is kx , where x is the vertical displacement of the simulated spring system due to the deflection of the composite material. (b) Experimental setup for measuring the attractive and repulsive forces generated by the material. When the electromagnet is powered, the material is either attracted or repulsed by the magnetic field. The material either pulls or pushes on the plunger, which transfers the force to the force sensor.

3.2.2.3 Force Testing

To evaluate the force transfer capability of our composite material and compare it to other typically used elastomers in haptics and robotics (Ecoflex 00-10, Ecoflex 00-30, Ecoflex 00-50, and Dragon Skin 30), we built the experimental setup shown in Fig. 3.8. The setup is comprised of an electromagnet supported on a bracket above a sample of the composite material clamped at two of its edges, mounted on a 3-D printed plunger that transfers the force from the material to a 5N Wheatstone bridge force sensor (Honeywell FSG005WNPB). The purpose of the plunger is to transfer force to the sensor while separating it from the electromagnet to avoid interference with the sensor's circuitry; the measured field from the electromagnet at the location of the force sensor is zero.

For each material in the comparative study, we manufactured 6.5 mm-thick samples weighing $27.4 \pm 0.5\text{g}$. All samples had a 1:1 ratio by mass between the elastomer and the magnetic particle load. We also characterized the remanent magnetic field for each sample using a Gaussmeter and probe (FW Bell 5180). The remanent magnetic field of the BCP Oleogel is 3 times higher than in the other polymer composites (Table 3.1). This is likely a result of the more efficient particle chaining during gelation. When performing the force test, we placed the tip of the pole piece 5 mm above the material and recorded the change in force observed while driving

Table 3.1: Modulus data (without particles) and remanent field data (with particles) for different elastomers. All modulus data except for the oleogel data comes from the database associated with [43].

Material	Modulus E (kPa)	B Field (mT)
BCP Oleogel	0.3	9
Ecoflex 00-10	50	3
Ecoflex 00-30	165	3
Ecoflex 00-50	200	3
Dragon Skin 30	1120	2

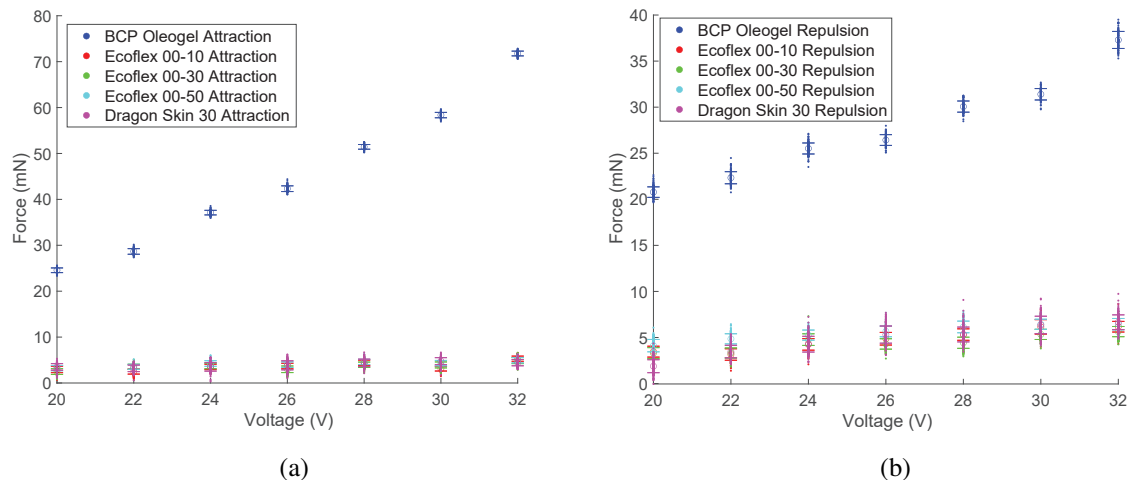


Figure 3.9: Force measurements for the attraction and repulsion of the selected material, the BCP oleogel made from Septon 4077 and Drakeol 34, versus the responses of Ecoflex 00-10, Ecoflex 00-30, Ecoflex 00-50, and Dragon Skin 30 with respect to the magnet. Error bars indicate the standard deviation of the data. **(a)** Force measurements under the attraction modality. **(b)** Force measurements under the repulsion modality.

the electromagnet between 20-32 V, which is also the range we used in Section 3.3 to actuate the finger sheath. Fig. 3.9 shows the relationship between voltage and force for attraction and repulsion of the five comparative samples. The oleogel force outputs are on the order of cN while the force outputs of the other four materials exhibit force outputs on the order of mN. In comparing the oleogel composite sample and the other samples, there is a force difference of least 1 cN at an input of 20 V. At 32 V, the difference is at least 5 cN. This is likely due to a combination of the lower material modulus of the oleogel and the higher remanent magnetic field in the material. For the oleogel, both the attraction and repulsion modalities exhibit a monotonic increase with respect to voltage. The attractive force is approximately twice as high as the repulsive force, likely due to the increased magnetic force on the material as it deflects and moves closer to the magnet.

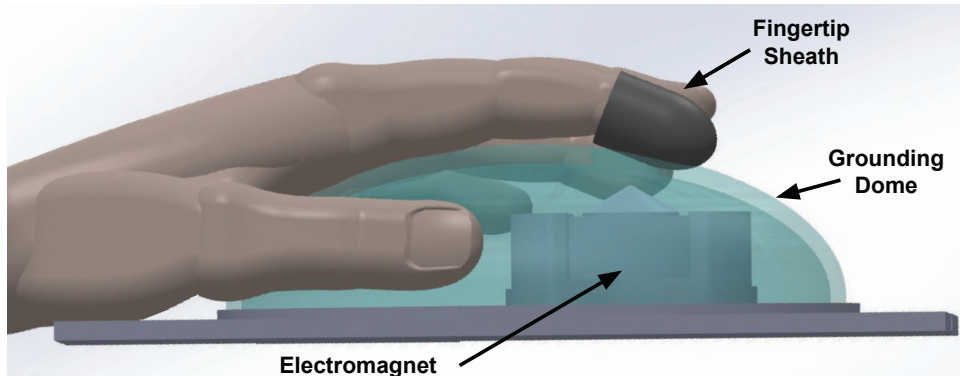


Figure 3.10: Experiment setup: the finger of the user rests above a small opening the grounding dome while the electromagnet sits under the dome to provide actuation forces.

3.3 Psychophysical Validation

3.3.1 Experiment: User Perception of Sensation Intensity

The purpose of this experiment was to characterize the perceptual intensity of the force transmitted from the sheath to the user as a function of the voltage input into the electromagnet. To evaluate the device for future applications, we wanted not only to ensure that the user discriminated between signals, but also to determine whether perceived intensity increased systematically with increases in voltage. Since the material can exhibit both attractive and repulsive behavior with respect to the electromagnet, we also wanted to test these two different modalities to evaluate their impact on perception.

3.3.2 Method

Seventeen subjects (thirteen male, three female, and one who chose not to specify a gender) participated. They were between the ages of nineteen and twenty-nine and came from the community at Carnegie Mellon University. All were right-handed. The Carnegie Mellon University Institutional Review Board approved this study under IRB ID STUDY2022-00000048. At the beginning of the experiment, the experimenter demonstrated how to wear the fingertip sheath in the correct orientation, with the polarity of the material aligned north-south with respect to the distal and proximal regions of their fingertip, in order to feel attraction vs. repulsion. To minimize the kinesthetic effects of pushing or pulling on the joint of the fingertip, each subject rested their hand on a dome that covered the electromagnet. The dome (Fig. 3.10) is an 3D-printed PLA structure that grounds the user's hand with a 1 cm^2 fingertip-shaped hole for the user to place their index finger $\approx 5\text{ mm}$ above the electromagnet and to allow clear perception of the magnetic field. Subjects wore noise-cancelling headphones playing pink noise for the duration of the experiment to prevent auditory cues from the experimental setup.

The experiment consisted of two procedurally identical sessions: one to test the attraction

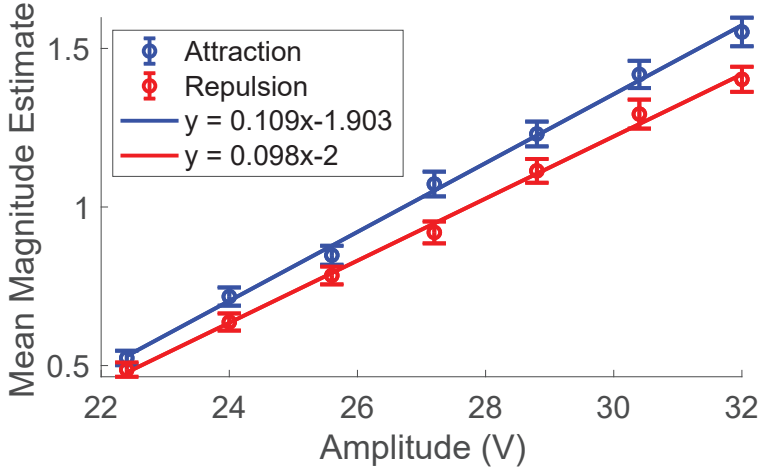


Figure 3.11: The average normalized magnitude estimate responses with standard errors. Both modalities, attraction and repulsion, exhibit linear relationships between voltage input and mean magnitude estimate.

modality and one to test the repulsion modality of the electromagnet and sheath. The subjects were not told that there was any difference between the two sessions. The order of the two sessions was randomized among subjects to avoid any biasing effects due to familiarity with the interface. Each session consisted of a series of 7 discrete voltage amplitudes supplied to the electromagnet, presented in 10 unique permutations, for a total of 70 stimuli per session. The subject pressed an icon in the experiment's graphical user interface (GUI) to play each stimulus at 4 Hz for 5 seconds, and the subject could choose to replay the stimulus as many times as they wished. After playing the stimulus, the subject entered a number into a text box in the GUI corresponding to their interpretation of the intensity of the sensation. The experimenter told each subject to choose their own range, as long as they excluded negative numbers and only selected 0 when no sensation was perceived. They were instructed to associate higher numbers with higher levels of intensity. This task, known as free magnitude estimation [88], has been used previously in the characterization of tactile haptic devices to correlate physical stimuli with psychophysical perception [51].

3.3.3 Results and Interpretation

Following the analysis in [51], we normalized the responses of each subject by dividing each of their responses to a given voltage input by the average of all of the responses of that subject to both the attraction and repulsion stimuli in order to compare any effects due to the different modalities. The cumulative dataset of average normalized response to voltage follows a linear relationship, with the R^2 value of the linear fit being > 0.99 for both experiments.

The linear trend was also present in individuals' data, with average R^2 values of 0.93 for repulsion and 0.94 for attraction. The fit makes sense in this case since a linear fit has also been reported for magnitude estimation with respect to normal force (between 0.22-0.75 N) application to the fingertip, with $0.49 \leq R^2 \leq 0.94$ for seven subjects considered separately [55]. We performed a two-factor analysis of variance (voltage and actuation mode) on the normalized data and found that the sole effect was that of voltage ($p < 0.001$). Repulsion and attraction showed no mean difference (i.e., no main effect of actuation mode) and the voltage effect was statistically equivalent for attraction and repulsion (i.e., no interaction between factors). Additionally, t-tests comparing the slopes for repulsion and attraction failed to reach significance. This indicates that the subjects did not differentiate between the two modes of actuation. This is notable in that the forces measured in Section 4.2 were up to twice as high in the attraction modality as in the repulsion modality. This result may be due to the fact that the subjects could have been self-normalizing their ranges within each session.

3.4 Conclusions

In this chapter, we presented and tested a novel tactile haptic device composed of a wearable fingertip sheath and an external electromagnet. The electromagnet was equipped with a pole piece designed to focus the highest possible magnetic field over a desired area of the material. The fingertip sheath was fabricated using a BCP oleogel composite specifically designed to maximize the deformation of the material in the direction of an externally applied magnetic field, as well as the force transfer to the fingertip. We compared this material to composites created with commonly used elastomers in robotics and haptics applications and found that the force generated by our BCP oleogel-based composite over a range of excitation voltages to an electromagnet was an order of magnitude greater than those generated by the other materials. Through psychophysical testing, we showed that users felt a range of sensations linearly proportional to electromagnet voltage input and that they could not differentiate between the tactile sensations of attraction and repulsion as provided by the sheath. Overall, the totality of our findings indicated that this initial device had the potential for use in a more advanced texture-rendering device, leading us to develop the platform discussed in Chapter 4.

Chapter 4

MAGTRACE: An Electromagnetic Texture Rendering Platform

In this chapter, we discuss the successor device to the sheath and electromagnet paradigm introduced in Chapter 3. We call this device MAGTRACE, which stands for MAGnetic Texture Rendering for Active Contact and Exploration. MAGTRACE is a novel texture display platform that features a wearable magnetic fingertip sheath together with a set of electromagnets mounted on a low-friction linear rail, driven back and forth by the user while their fingertip is actuated between the electromagnets. The design of this device draws on elements from the broader body of magnetic haptics research and extends this existing paradigm toward an application in macroscale texture display. We achieve this by adding lateral motion to the magnetic setup, allowing for the creation of a distally attributed environment in which the user can explore virtual electromagnetically rendered textures [32, 37, 40, 41, 68]. We also present results from a user study that evaluates the utility of the device for emulating textured surfaces. Users were asked to identify which of three waveform shapes (sine, square, triangle) composed a presented surface at sizes 1, 2, 4, and 6 mm. The results establish that using these baseline textures as a toolbox, this actuation modality can effectively serve as a platform for texture rendering at the macroscale, where elements of shape and size can be differentiated. Furthermore, these results determine parameters of shape and scale that can help facilitate discrimination during texture rendering.

The main contributions of this chapter are as follows:

1. The MAGTRACE platform and its actuation and exploratory mechanisms (Sec. 4.1, 4.2).
2. Experimental results indicating that MAGTRACE produces differentiable macroscale texture environments, specifically shapes, and that users were able to consistently identify waveform shapes with varying sizes at rates above 80% (Sec. 4.3.3).

4.1 Device Overview

MAGTRACE consists of three main elements:

1. A dipole **magnetic fingertip sheath** worn by the user on their index finger (Fig. 4.1)

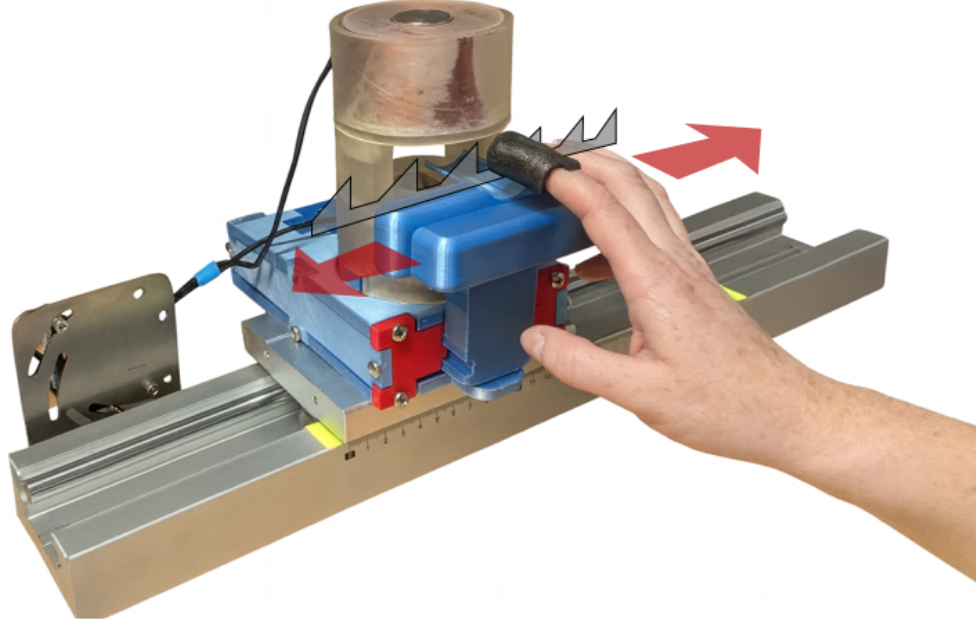


Figure 4.1: MAGTRACE: A linear exploration platform for magnetic fingertip actuation using dual electromagnets mounted on a low-friction sliding carriage. Here, the user holds their hand outside of the magnet apparatus, showing the magnetic fingertip sheath on their index finger.

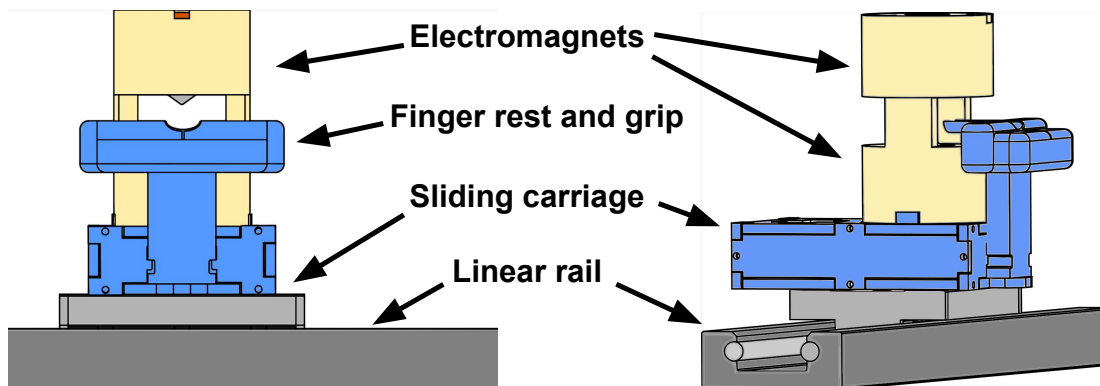


Figure 4.2: Detailed view of the linear texture exploration platform, consisting of two center-focused electromagnets (held inside the yellow housing) mounted on a sliding carriage with a handle for the user to drive it bidirectionally across a linear rail as the magnets render virtual textures.

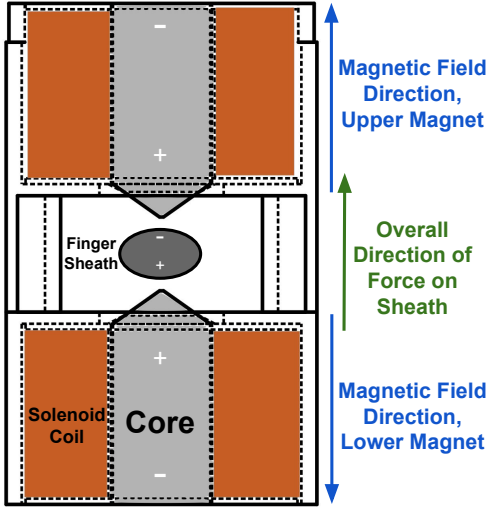


Figure 4.3: Detail of dual electromagnet setup, consisting of two identical electromagnets placed opposite to one another, with the finger sheath in between. The field directions of the electromagnets were chosen such that the bottom magnet repulses the sheath and the top magnet attracts it and the upward force on the sheath is maximized.

2. A **set of two electromagnets** arranged so that their respective fields are concentrated on the sheath (Fig. 4.2)
3. A **slider handle and finger rest** on a linear rail for the user to move the sliding carriage holding the electromagnets while maintaining the position of their fingertip in the concentrated magnetic field (Fig. 4.3)

According to the taxonomy presented in [54], the independent wearability of the sheath and the tabletop implementation of the electromagnets mounted on the linear rail imply that the presented platform falls somewhere along the spectrum between grounded and wearable fingertip haptic devices; the user may move their hand freely while wearing the sheath and does not need to be strapped into the electromagnet apparatus, but they must grasp the handle of the carriage holding the electromagnets in order to properly experience the actuation. In this case, MAGTRACE combines the research on magnetic fingertip actuation described in Section 2 with a more developed tabletop peripheral setup in order to display macroscale textures.

4.2 Design and Characterization

4.2.1 Wearable Magnetic Fingertip Sheath

The purpose of the fingertip sheath was to provide the user with direct actuation of the fingertip: as the electromagnets generate a force between themselves and the sheath, this force is in turn transferred to the user. The sheath was constructed from a combination of magnetic neodymium alloy (Nd-Pr-Fe-B) particles (Magnequench MQP-AA4-15-7, 150 mesh, flake geometry), white mineral oil (Penreco Drakeol 34), and a combination of two grades of a triblock copolymer (Ku-

rary Septon 4033, Septon 4055) that crosslinks within the oil to create an oleogel. The elastomer resulting from the combination of the copolymer and the mineral oil was originally developed for use in prosthetics and other medical devices, and so is safe for direct contact with human skin [56]. During the gelation of the material, we exposed the sheath to a constant magnetic field in the direction of the cross section of the fingertip, resulting in a weak permanent magnetic field across the sheath. At the surface of the sheath, we measured the remanent magnetic field to be approximately 0.03 T.

Specifically, the magnetic fingertip sheaths used in this work consisted of Septon 4055 (1 wt%), Septon 4033 (4 wt%), white mineral oil (45 wt%), and neodymium alloy particles (50 wt%). We combined these components in the chamber of a twin-screw microcompounder (XPlore MC 15 HT) and processed them at 250°C at 100 rpm with applied torque 5 Nm for 15 minutes prior to extrusion into the finger sheath mold and placed the mold in a holder in which the sheath was suspended in a uniform magnetic field created by two 2" × 2" × 1" N52 neodymium alloy permanent magnets. All sheaths were approximately 3 mm thick and 40 mm in length.

4.2.2 Electromagnetic Actuation

The design goal for the electromagnet setup was to drive the two electromagnets simultaneously with the effect of producing the maximum possible upward force on the fingertip. While driving the direction of the current such that each electromagnet generated a magnetic field in the same direction would produce maximum magnetic field strength in between the magnets, this would not actually produce the highest force on the fingertip, as the sheath's poles would instead cause it to be pushed upward by one magnet and downward by the other, canceling the net directional force. Instead, as shown in Fig. 4.2, the more optimal approach is to direct the current so that the overall fields of each magnet travel in opposing directions in order to repulse the sheath from below and attract it from above.

The electromagnets themselves consisted of a high-saturation magnetic core (Vacoflux 50, Goodfellow) custom-machined to the optimal pole piece angle (54.7°) described in [34] for maximum focusing of the magnetic field, 3000 turns of enameled copper wire (CNC Tech 26 AWG), and a bobbin that was printed using heat-resistant resin (Formlabs High Temp Resin), chosen in order to avoid melting of the housing during use. These electromagnets follow a design similar to the device presented in the previous chapter, but improve on that design by using one machined rod for both the core and pole piece to avoid material mismatch and corner flux leakage, as well as a better suited choice of core material for our desired use case involving lower-frequency activation and higher flux output. We drove the electromagnets using an Arduino Uno microcontroller with a custom shield using the DRV8840 H-Bridge motor driver chip (Texas Instruments) rated for voltages up to 45 V and currents up to 6 A, to power the electromagnets at typical ranges during use of up to 40 V and 2 A. We measured the magnetic flux at the midpoint between the two magnets to be about 0.01 T when the magnets were driven at 40 V.

4.2.3 Linear Rail and Sliding Exploration Platform

The purpose of mounting the electromagnets on a linear sliding mechanism was to allow the user to freely explore the displayed virtual textures. We used a 20-inch linear bearing slide rail with an adjustable-friction carriage (Firgelli Automations FA-SGR-35-20). We selected this type of rail and carriage because of its low friction and low vibration, since greater friction and vibration would detract from the user's ability to differentiate between textures by creating unintended force signals in addition to those generated by the electromagnets. To further eliminate friction generated from a potentially off-balance carriage, the section opposite from the handle was weighted internally with leadshot encased in silicone. The handle and carriage mount were all 3D printed using PLA. To calculate the position of the user, we mounted a laser range finder (SICK OD2-N120W60U2) parallel to the rail with its laser directed towards the carriage. The readings from the laser were sent in analog form to the microcontroller to calculate the appropriate electromagnet voltage with respect to user position.

4.2.4 Spatial Rendering of Magnetic Force

As explained in Section 4.2.2, the actuation strategy used to convey maximum upward force to the fingertip involved repulsing the magnetic sheath with the lower electromagnet and attracting it with the upper electromagnet. Combining this effect with the spatial information provided by the laser range finder, we sought to replicate the sensation of moving one's fingertip across an uneven surface by varying the field strength of the electromagnets depending on the location of the fingertip along the rendered environment. Specifically, we calculated the unit-scaled amplitude A for the output voltage in terms of the range finder distance x and desired spacing $S \in \{2, 4, 6\}$ for each waveform shape as follows:

Sine:

$$A(x) = \begin{cases} \sin 2\pi x f, & \text{if } \sin 2\pi x f \geq 0 \\ 0, & \text{otherwise} \end{cases}$$

Sawtooth:

$$A(x) = \begin{cases} \frac{x \bmod S}{L}, & \text{if } x \bmod 2S \leq S \\ 0, & \text{otherwise} \end{cases}$$

Square:

$$A(x) = \begin{cases} 1, & \text{if } x \bmod 2S \leq S \\ 0, & \text{otherwise} \end{cases}$$

where for the sine waveform, frequency $f = \frac{1}{2S}$, and for both the square and sine waveforms, \bmod was implemented as the floating-point remainder function. Each texture was 90 mm in length, with the total traversable distance being 100 mm. The input voltage during all experiments was 40 V. These waveform shapes were chosen for the purpose of being “building blocks”

towards other textures, as they can be combined to make more complex texture environments. The relevance of these shapes is supported by previous haptic research; for example, the authors of [11] implemented and tested similar waveforms on an ultrasonic surface vibration platform, generating the waveforms across a spatial range of 0 to 6 mm.

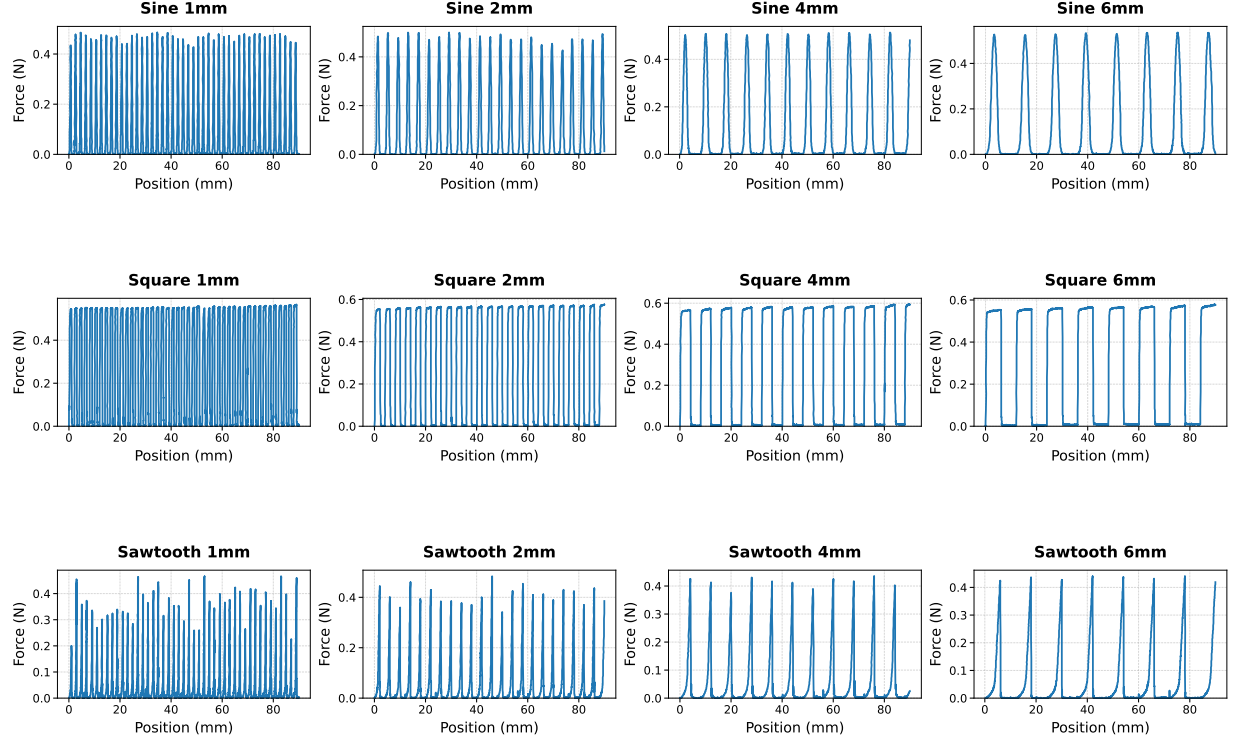


Figure 4.4: Force testing data demonstrating the response of an aluminum bending beam force sensor with magnetic sheath on the tip moving through the twelve stimuli defined by size and shape and rendered in user tests, as described in Sec. 4.2.5. The waveform shapes are generated by the PWM input described in Section 4.2.4.

4.2.5 Validation of Rendering

In order to test the efficacy of the system in rendering nine specific textures, we tested the response of a cantilever force probe (EBB-1 Bending Beam Force Sensor, Transducer Techniques) moving through the virtual environment with the same method of fingertip actuation explained in Sec. 4.2.2. We placed the larger of the two sheaths used in the user studies described in Section 4.3.3 on the end of the cantilever probe and drove the carriage manually through each of the twelve virtual environments. Fig. 4.4 shows the analog response of the probe with respect to its position as it moves along the linear rail. To reduce sensor noise, we applied active filtering in the form of a first-order low-pass filter, specifically $y[n] = \alpha x[n] + (1 - \alpha)y[n - 1]$. Although there were some issues with consistent sampling at the lower spacings, especially for the sawtooth

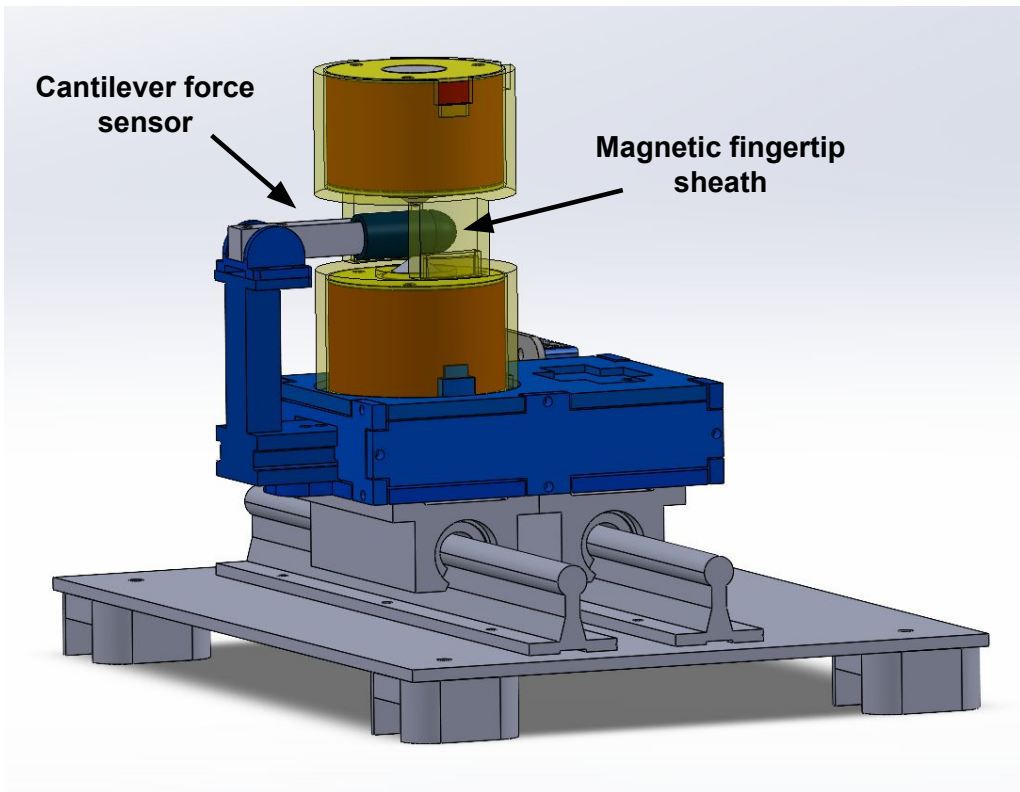


Figure 4.5: Force testing setup consisting of a cantilever-style bending beam load cell with the magnetic fingertip sheath on the end. This experimental setup was used to capture the data in Fig. 4.4.

waveform, which hits its maximum only very briefly and thus can be difficult to accurately sample, the data shows that the applied forces on the sheath consistently reached approximately 0.5 N in the sine and square environments, and approximately 0.4 N in the sawtooth environments, with waveform shapes corresponding to the voltage input described in Section 4.2.4.

4.3 User Interaction Study

The validation of rendering described above indicates that MAGTRACE has the potential to render three discriminable waveforms at a range of spacings. Analysis of user interaction is needed, however, to evaluate whether the waveforms can be perceptually differentiated. An interaction study described next addressed this question with the task of absolute identification, which requires not only discrimination but categorical recognition.

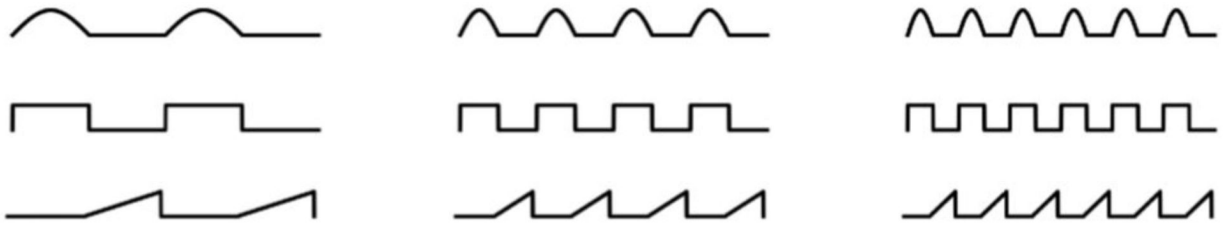


Figure 4.6: Iconographic depictions of nine texture stimuli presented to users in the GUI during the exploratory study. Each icon corresponds to a stimulus defined by size and shape, rendered by the device.

4.3.1 Stimulus Factors

The study assessed size and shape as independent factors of the rendered stimuli. An initial exploratory study manipulated each variable at three levels and asked users to identify both features of the rendered stimulus, in order to provide preliminary data about MAGTRACE’s effectiveness. The main study isolated each size to assess shape identification across a broader range of sizes.

- 1. Waveform Shape:** As demonstrated in Section 4.2.5, the device can be commanded to produce varying levels of force by supplying different levels of voltage to the electromagnets. Three waveform shapes were rendered: a sine wave, a square wave, and a sawtooth wave, each with non-positive parts of the waveform mapped to zero.
- 2. Feature Width and Spacing:** For each of the waveform shapes, we scaled the strictly positive portions of the waveform to be the same length as the zero-amplitude portions that separated them. Each shape was presented as the positive section of the waveform, with the negative section mapped to zero amplitude, resulting in nonzero amplitude sections and zero amplitude sections (spacings) of equal length. These spacings could then be scaled to targeted values.

4.3.2 Preliminary Exploratory Experiment

The preliminary study was intended as an efficient exploration of the space of renderings defined by the stimulus factors of shape and size. The waveform shapes were those previously evaluated for rendering: square wave, sine wave, and sawtooth. Each was rendered at three discrete spacings: 2 mm, 4 mm, and 6 mm. The three waveform shapes and three spacings were permuted into nine discrete stimuli to be presented to the user, each of which was presented ten times for a total of ninety trials. The stimuli were presented as consecutive permuted lists, resulting in each of the nine stimuli being presented once per nine trials. In each trial, the user compared the stimulus rendered by the device with nine iconographic depictions of the entire set (Fig. 4.6) and was asked to identify which of the icons corresponded most closely to the physical stimulus. The Carnegie Mellon University Institutional Review Board approved this study under RB ID STUDY2022-00000048.

4.3.2.1 Exploratory Experiment Methods and Procedure

Eleven subjects participated in this part of the study. Four subjects were female, six were male, and one chose not to specify a gender. They were between the ages of twenty-one and twenty-nine and all were right-handed. At the beginning of the experiment, the experimenter gave explicit instructions to the subject that they should try to move the slider carriage at a constant speed in a single direction until reaching the bounds of the virtual environment, at which point they were permitted to reverse direction to explore the environment further. The bounds were marked visually on the slider component of the device, and the desired speed was demonstrated visually and aurally by a metronome set to 60 bpm and placed in the sightline of the subject (the subject was instructed to traverse the 100 mm of the test area in the space of 4 beats, resulting in a speed of 25 mm/s). The experimenter also provided the subject with a brief demonstration of the use of the slider and assisted the subject in the correct placement of the sheath on the right index finger, so as to make sure that the poles of the sheath sat in the correct alignment for the desired up-and-down actuation. Once the sheath was situated, the subject grasped the slider handle with their right hand, extending their right index finger along the finger rest, and placed their left hand on the mouse peripheral of the computer to be used for the duration of the session.

Prior to starting the experiment, the subject familiarized themselves with the possible stimuli via a self-driven training module. In this module, the subject used a graphical user interface (GUI) in which after the selection of one of the iconographic representations (Fig. 4.6), the device rendered the corresponding stimulus for the subject to explore in the manner initially demonstrated by the experimenter. The experimenter instructed the subject to explore each stimulus at least once before concluding use of the training module, and encouraged the subject to switch back and forth between environments to compare. The subject was permitted to train for as long as they wished before proceeding with the session and could ask the experimenter questions during the training. After training, the subject began the experimental portion of the session. During this time, they wore noise-canceling headphones playing pink noise to avoid any auditory cues presented by the electronics. The device rendered each stimulus as described in Sec. 4.3.2, and the subject was allowed to take as long as they wanted to explore the stimulus before using the GUI to select which of the nine iconographic depictions they believed best corresponded to the rendered stimulus. The program prompted the subject to confirm their selection, at which point the GUI displayed a transitional screen for three seconds before proceeding to the next stimulus.

4.3.2.2 Exploratory Experiment Results and Discussion

Considering accuracy of identifying the stimulus correctly with respect to both shape and spacing, fully correct identification was about 48% for all shapes and spacing lengths. (With 330 responses, 48% exceeds the 33% chance level for each shape and texture by proportion test, $p < 0.001$). Identification of waveform without regard to correct spacing was correct about 69% of the time. In the case of spacing identification, however, the breakdown was less uniform across waveform types. While subjects were able to correctly identify a surface as having 2 mm spacing about 87% of the time, they could identify a stimulus as having 4 mm spacing about 66% of the time, and as having 6 mm spacing 60% of the time. Confusions were also spacing

dependent: while the 2 mm and 6 mm stimuli were discriminated with high accuracy, responses to 6 mm stimuli deviated toward the lesser value of 4 mm about 36% of the time, indicating that the device could not consistently provide the user with cues sufficient to differentiate between the 4 mm and 6 mm textures.

Overall, subjects tended to make errors that matched the target in either shape or size, but they differed with respect to absolute accuracy, as shown in Figure 4.7. The subject data is presented in the form of a set of two-factor confusion matrices, in which the diagonal of each of the eleven subject matrices shows the responses that were correct with respect to both shape and spacing. The group on the left of the figure is largely clustered on the diagonal and the remainder shows a broader range of off-diagonal errors. It seemed possible that this variability results from the sheath fitting some individuals' fingertips better than others, or from some users being inadequately trained with respect to the discriminations required. Table 4.2 summarizes some relevant post-study questionnaire responses, given on a scale between 1 (Strongly Disagree) and 7 (Strongly Agree), of the higher-performing group (those on the left-hand side of Figure 4.7) versus the lower-performing group. The answers indicated that the higher-performing group generally felt less discomfort and fatigue during the study, while the lower-performing group felt that the study was more physically and mentally demanding.

		Rendered Environment								
		ST2	ST4	ST6	SN2	SN4	SN6	SQ2	SQ4	SQ6
Selected Environment	ST2	46	6	0	27	3	0	7	4	0
	ST4	16	45	24	2	11	7	0	10	8
	ST6	0	22	62	0	2	8	0	2	1
	SN2	26	5	1	52	13	2	33	7	3
	SN4	4	22	7	10	60	25	2	8	7
	SN6	0	2	11	1	10	54	1	1	3
	SQ2	14	1	0	17	1	3	64	21	4
	SQ4	4	5	2	1	10	6	3	46	33
	SQ6	0	2	3	0	0	5	0	11	51

Table 4.1: Two-factor (shape, spacing) confusion matrix presenting the aggregate data for the environment rendered by the device vs. the environment selected by the subject in the exploratory study. Variable key: **ST2 ... ST6**: sawtooth wave 2mm ... 6mm, **SN2 ... SN6**: sine wave 2mm ... 6mm, **SQ2 ... SQ6**: square wave 2mm ... 6mm. Correct responses are highlighted in blue.

4.3.3 Main User Interaction Study

The exploratory study showed promise for MAGTRACE as a tool for rendering textural environments with specific sizes and shapes. However, there were strong individual differences in performance, and the lower-performing group reported greater physical and cognitive demand

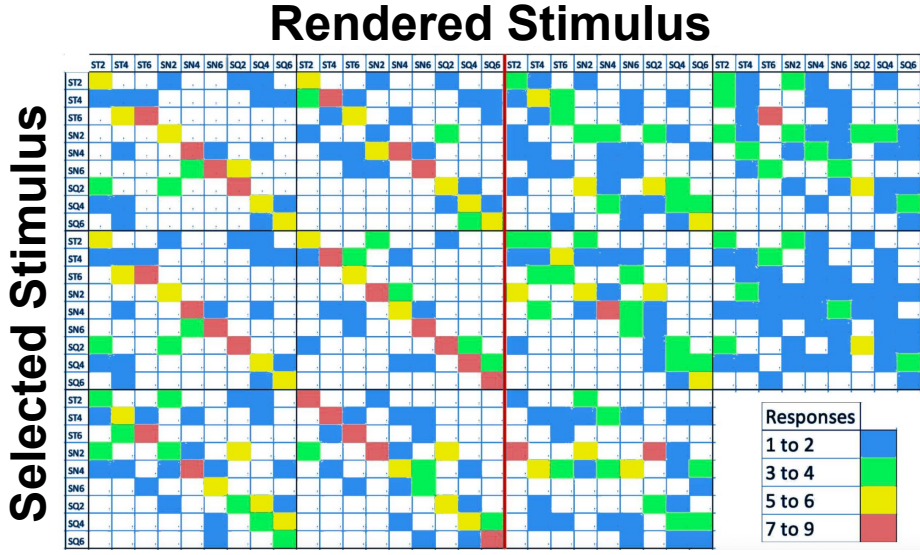


Figure 4.7: Individual confusion matrices for each of the eleven study participants. Columns are rendered stimulus environment; rows are responses. The color of each box represents the number of responses of that type. The matrices on the left side of the red line represent the higher-performing group (HPG) of subjects, while those on the right represent the lower-performing group (LPG). ST = sawtooth, SN = sine, SQ = square, and associated numbers are spacing in mm.

Post-Study Questionnaire Prompt	HPG Avg	LPG Avg
I experienced undue fatigue/discomfort during the study	3.5	5.4
The study was mentally demanding	3	5.2
The study was physically demanding	1.67	3.2
The study was annoying	1.83	3.6
I felt distracted at some point during the study	2	4

Table 4.2: Post-study questionnaire results for the higher-performing group (HPG) and lower-performing group (LPG). Each prompt was answered with an integer between 1 (Strongly Disagree) and 7 (Strongly Agree).

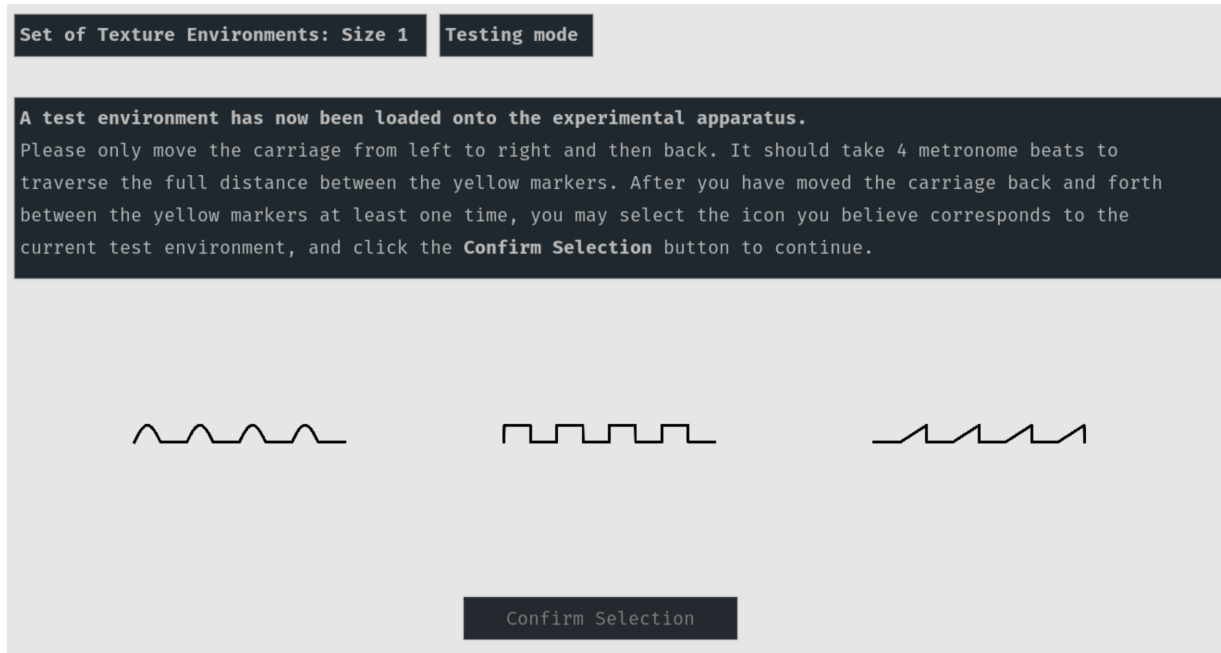


Figure 4.8: GUI for the main user interaction study, in which the user only had to pick from three icons during each trial, instead of nine icons as in the exploratory study.

(see Table 4.2). Given these positive findings and limitations, the main experiment assessed shape recognition at a specific size, varying size across testing blocks to determine the scales at which discrimination would be successful. We believed that the reduction to a three-alternative identification should reduce cognitive load, in accordance with the questionnaire results. Additional modifications were made to assess the fit of the device to the individual user and to expand training.

The magnetic stimuli in the main study were rendered identically to those in the exploratory study, but instead of the user being made to choose between nine icons representing nine environments at once, the experiment was split into sections, during which only waveforms with a single spacing length were presented. During these sections, the user was prompted to identify the waveforms as being either sine, sawtooth, or square waves by selecting one of three icons representing the waveform shape. The section orders were randomized in Latin square form in order to minimize practice effects. In a given section, the three stimuli were presented as consecutive permuted lists, with each stimulus appearing ten times over the course of the section. Additionally, we conducted two sets of experiments to better understand the users' ability to discriminate over coarser and finer textures; the first group was tested on three separate sections with the same spacings as in the exploratory study (2 mm, 4 mm, 6 mm), while the second group was tested on sections with spacings of lengths 1 mm and 2 mm, respectively.

4.3.3.1 Main Experiment Methods and Procedure

In order to mitigate the possible sources of error in the exploratory study described previously, changes were made as outlined below; otherwise, the experimental procedure remained identical to the previous one.

1. **Multiple Sheath Sizes:** In the exploratory study, only one size of sheath was available to users (13 mm inner diameter). The current study allowed the users to choose between the original size and a larger size (16 mm inner diameter). In addition, to make sure the sheath performed as expected, we implemented a sizing pretest in which the user tried on their preferred size of sheath and then used it to determine a number of square wave pulses (between one and three, rendered at 4 Hz) over ten trials. If the user got eight or more correct, the experiment proceeded using that sheath size.
2. **Extended Training:** During the exploratory study, training consisted of letting the user select between the nine stimuli to compare and contrast. In order to make sure that the users had sufficient familiarity with the interface before starting the testing phase of the experiment, we extended the training to include a guided training, in which the users were specifically directed to explore each of the three environments presented in a given section, then to explore each environment a consecutive time, and then finally to freely compare and contrast between the environments. This training preceded each of the experimental sections.

The first group of users, which was tested on spacings of lengths 2 mm, 4 mm, and 6 mm, consisted of eighteen subjects between the ages of twenty and forty-four. Six were female and twelve were male. Seventeen of these subjects were right-handed and one was ambidextrous. The second group, which was tested on spacing lengths of 1 mm and 2 mm, consisted of twelve subjects (all unique from the first group) between the ages of twenty and thirty-four. Three were female, eight were male, and one chose not to specify a gender. Ten of these subjects were right-handed and two were left-handed. All subjects used their right hand to operate the device during the experiment. Although some users had taken part in the exploratory study, the main study took place about ten months afterward, and any effects from previous use of the device should be minimal.

4.3.3.2 Main Experiment Results and Discussion

For the first group of participants, shown in Table 4.3, the overall average accuracy in discriminating between waveform shapes in the 2 mm, 4 mm, and 6 mm spacing lengths was near 87%. Within the sections, accuracy for 2 mm spacings was 83%, for 4 mm spacings was 88%, and for 6 mm spacings was 90%. No bias was observed towards any particular waveform. For the second group of participants, shown in Table 4.4, the accuracy for 2 mm spacings was identical to that observed in the first group (83%), and the accuracy for 1 mm spacings was 81%. These results are summarized in Fig. 4.9, in which we can see that users made similar amounts of total errors at sizes 1 and 2 mm, and improved further as spacing size increased. The decrease in errors from 2-6 mm spacing was confirmed by within-subject Analysis of Variance on data from

		Rendered Environment								
		SN2	ST2	SQ2	SN4	ST4	SQ4	SN6	ST6	SQ6
ID	sine	146	31	18	171	21	2	165	15	6
	saw	18	142	9	5	155	28	12	163	15
	square	16	7	153	4	4	150	3	2	159

Table 4.3: Confusion matrix presenting the aggregate data for the first group of subjects in the main user study. Variable labels as in Fig. 4.7.

		Rendered Environment					
		SN1	ST1	SQ1	SN2	ST2	SQ2
ID	sine	89	13	14	94	15	14
	saw	10	105	7	10	98	4
	square	21	2	99	16	7	102

Table 4.4: Confusion matrix for the aggregate data for the second group of subjects in the main user study.

the first group of users ($p = 0.02$).

An additional observation is that at certain spacing sizes, some of the waveform shapes may be confused with one another more than others. At the 4 mm and 6 mm spacing sizes, the errors were too sparse for sufficient analysis, averaging less than 0.5 per person for some shape combinations (meaning that there was no confusion trend to test), and the confusion matrices were not symmetric enough to fold together pairwise confused shapes. At 1 mm and 2 mm, however, there were sufficient errors and confusion matrix symmetry to make the confusion trend evident. Within-subject t-tests confirmed that there were significantly fewer confusions between sawtooth and square than between sine and sawtooth or between sine and square (at 1 mm, $p = 0.04$ and <0.01 ; at 2 mm with combined data from both user groups, $p < 0.01$ and $p = 0.02$, respectively; see Fig. 4.10).

To compare the data from the main user study with that of the exploratory study, we used the correction method recommended by the American Psychological Association to account for the change in difficulty going from a nine-choice discrimination task to a three-choice task [5]. Specifically, we rescaled each individual score x by using the guessing rate $1/n$, where n is the number of possible choice alternatives, such that $x \rightarrow x(1 - 1/n)$. For this comparison, we only considered the performance data of the top six participants from the exploratory study (the HPG). The raw and adjusted averages for each study are listed in Table 4.5. As the adjusted exploratory study average lies outside of the confidence interval range of the adjusted main study average in each category of spacings, we can conclude that the subjects in the main study showed overall improvement with respect to the exploratory study. This may be due to improvements in the training protocols and the better-fitting sheath options.

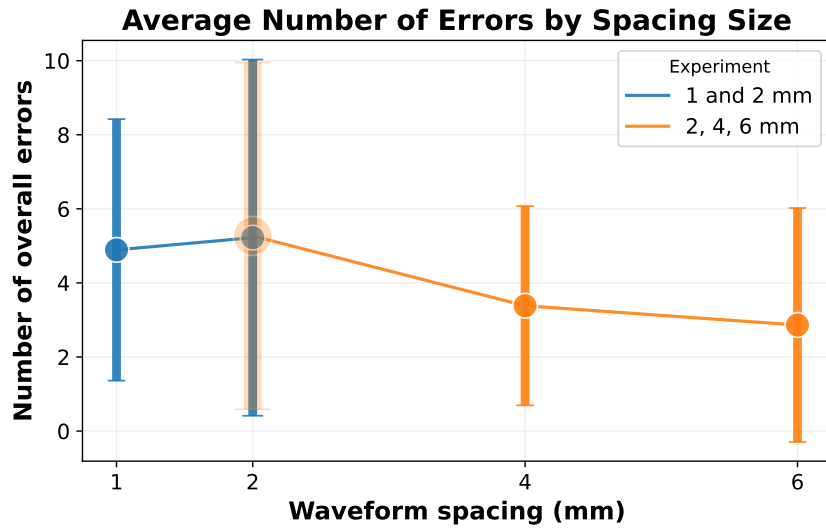


Figure 4.9: Average total errors made at each size of spacing in the main user study. The number of overall errors were observed to decrease as the spacing size increased. Error bars represent the standard deviations of the data.

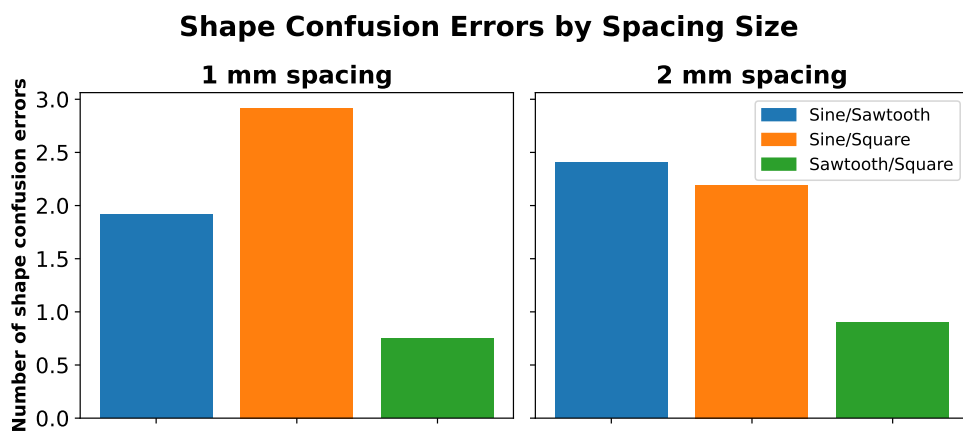


Figure 4.10: Average shape confusion errors for the 1 mm and 2 mm spacing conditions in the main user study. The majority of errors made at these sizes were between sine and square or sine and sawtooth.

	2 mm	4 mm	6 mm
Raw average for exploratory study	0.49	0.46	0.5
Raw average for updated study	0.83	0.88	0.9
Adjusted average for exploratory study	0.45	0.46	0.52
Adjusted average for main study	0.55	0.59	0.6
95% CI for main study	0.06	0.03	0.04

Table 4.5: The raw and adjusted averages of correct responses from the exploratory study and the main study. The confidence interval determined from the data indicates an improvement in identification accuracy between the exploratory and main studies.

4.4 Conclusions

MAGTRACE, the platform presented in this chapter, represents a novel contribution to the existing body of research on exploratory texture rendering. Building on previous work in materials development and characterization, we have successfully extended the capabilities of haptic magnetic fingertip actuation with a slider and carriage setup that allows the user to access distally attributed virtual environments. While previous work on haptic magnetic sheaths has mainly been focused on actuation of the sheath while the hand stays in one place, the linear sliding design of MAGTRACE incorporates exploratory mechanisms into its usage that allow for a more natural interaction with magnetically rendered shapes. We validated the waveform shape and spacing lengths using force measurements and were able to show that users could identify waveform shapes in wider spacing environments (6 mm) at a rate of 90%, with accuracy rates above 80% even as the spacing sizes went down to 1 mm. This indicates that, using only its dual-magnet actuator, MAGTRACE can render sensations varying from fine-grained to macroscale, making it a viable platform for creating complex haptic scenes for virtual reality or teleoperation applications. Future iterations on this platform could include additional electromagnets aimed towards the sheath at different angles in order to further enrich the experience by incorporating lateral force sensations into the rendered environments.

Chapter 5

Characterization and Evaluation of Magnetic Oleogels for Haptics and Soft Robotics

During the course of our work with magnetic elastomers, we have gained valuable insight into the fabrication and characterization of SEBS/SEEPS oleogels with and without magnetic particles, and believe that this insight has value for the chemical engineering and materials science communities. For example, although there are several existing studies [3, 23, 53] regarding the mechanical properties of SEBS/SEEPS oleogels, there is little existing research regarding their properties when mixed together, and while there exists some research regarding the magnetomechanical properties of SEBS/SEEPS combined with soft magnetic particles (e.g. carbonyl iron) [42, 58, 59], there is less known about the behavior of these oleogels when combined with hard (permanent) magnetic particles such as those used in the devices presented in Chapters 3 and 4. Additionally, as noted in Section 3.2.2.1, silicone polymers remain the material of choice for most soft haptics and soft robotics applications. Given our success in haptic device fabrication using oleogels, a careful investigation into their properties from the haptics/robotics viewpoint may help promote the use of these materials in this domain. By providing numerical values for the mechanical properties of these materials, we can help engineers create FEA simulations using SEBS/SEEPS oleogels and compare projected device performance in relation to silicone-based elastomers.

5.1 SEBS/SEEPS Copolymer Blends

5.1.1 Tensile Testing

To begin our investigation into the mechanical properties of SEBS/SEEPS BCP oleogels, we first considered blends of several grades of Septon from Kuraray Inc: 4033, 4055, 4077, 8006. We planned to combine two grades at a time in the weight percentages detailed in Table 5.1, resulting in a total of 66 desired sample varieties, and to test 3 dogbone samples to determine the elastic modulus for each variety. In the experiments, each sample was tested in accordance

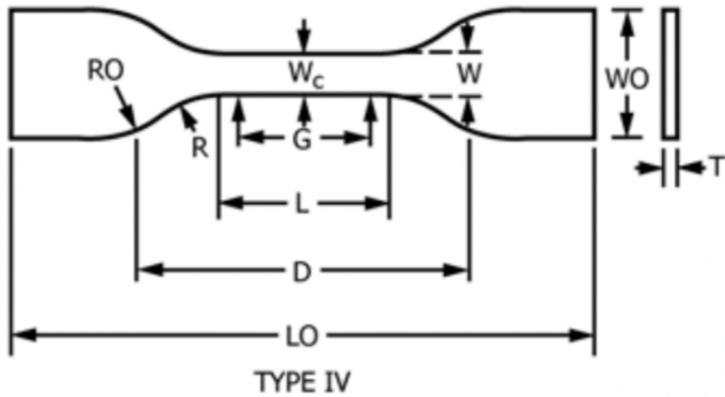


Figure 5.1: Dogbone dimension standard for a Type IV sample from ASTM Standard D638-22: Standard Test Method for Tensile Properties of Plastics.

	0%	5%	10%	15%
0%	N/A	5% S4077	10% S4077	15% S4077
5%	5% S4033	5% S4033, 5% S4077	5% S4033, 10% S4077	5% S4033, 15% S4077
10%	10% S4033	10% S4033, 5% S4077	10% S4033, 10% S4077	10% S4033, 15% S4077
15%	15% S4033	15% S4033, 5% S4077	15% S4033, 10% S4077	15% S4033, 15% S4077

Table 5.1: Example of planned testing samples combining Septon 4033 and Septon 4077, with total BCP weight percentages from 5% to 30%.

with ASTM Standard D638-22: Standard Test Method for Tensile Properties of Plastics. Samples were mixed for 15 minutes at 290°C with twin screw torque of 5 Nm and then extruded from the Xplore Microcomounder (MC 15 HT) into high temperature-resistant resin molds sized according to Figure 5.1 with width (W) 6 ± 0.5 mm, length (L) 33 ± 0.5 mm, width overall (WO) 19 ± 6.4 mm, and gauge (G) 25 ± 0.25 mm.

The results of this testing program are summarized in Tables 5.2 and 5.3. Out of the 66 desired combinations, 20 sample attempts failed to produce viable tensile testing samples, usually due to the fragility of the sample and its tearing while being removed from the dogbone mold. Out of these, 26 combinations resulted in at least 3 viable samples, giving us a reliable library of modulus data that can be used to select an oleogel formulation that corresponds to a desired elastic modulus. In particular, we have already used this library with our collaborators in order to develop more optimal types of interface materials for the further improvement of an ultrasonic encounter-type haptic device [63].

Analyzing the data from the 26 successfully tested oleogel combinations, we can begin to gain certain insights regarding the relationships between the makeup of the samples and their moduli. In Figure 5.2, we present the total polymer weight percentage (the rest being mineral oil) in a given sample vs. the elastic moduli, with further disambiguation based on which grade of Septon comprised the majority of that polymer weight. We can observe that overall, the

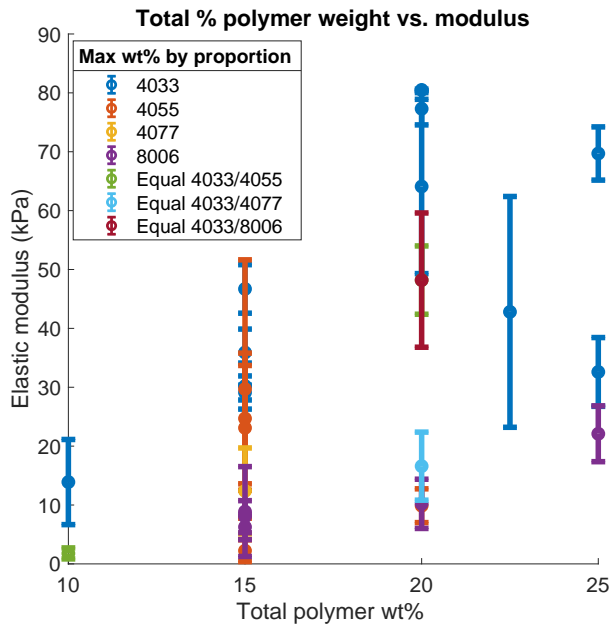


Figure 5.2: The total polymer weight percentage in a given sample vs. the elastic modulus of the sample. The remaining weight percentage in each formulation is made up of white mineral oil. The data regarding which grade of Septon comprised the majority of the polymer weight in each sample is also shown.

modulus increases as the total amount of Septon that makes up a sample increases, and that samples which are mostly made up of Septon grade 4033 generally have the highest moduli. In Figure 5.3, which shows the changes in elastic moduli as different grades of Septon are added to a constant baseline percent of Septon 4033, the data seems to indicate a slight decrease in modulus as greater amounts of Septon 4077 are added to the oleogel formulation, a counterintuitive result that may be of interest in future characterization tests.

5.1.2 Development of a ‘Matching Silicone’

In Section 3.2.2.3, we observed that the actuated force produced by the magnetic oleogel composite was consistently greater than that produced by composites made with silicones of varying moduli and the same weight percentage of magnetic particles. This result prompted several follow-on questions:

1. Could the differences in force output be due to the lower viscosity of the oleogel during gelation? Since ostensibly the remanent magnetism of a composite increases when the particles are in greater alignment, does it make sense that lower viscosity during the period in which the particles are free to move would contribute to overall particle alignment?
2. Alternatively, could the increased force output be related to the modulus of the base polymer? The moduli of the comparison silicones tested in Section 3.2.2.3 were all several orders of magnitude lower than the modulus of the tested oleogel.

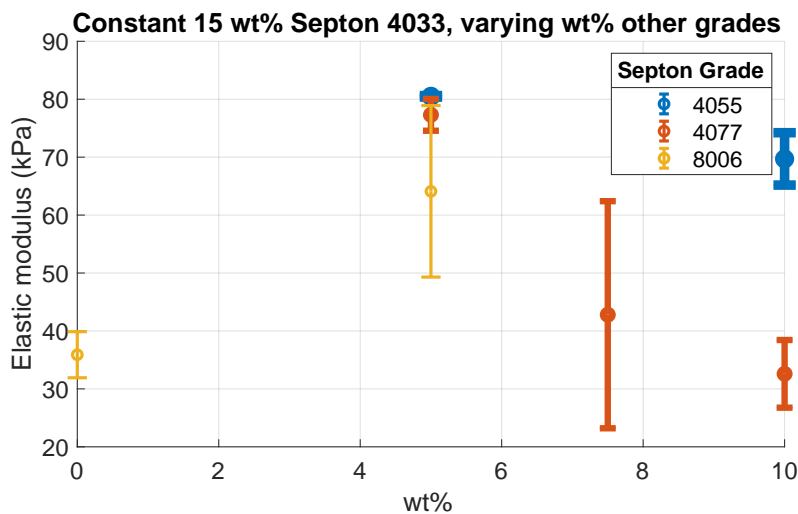
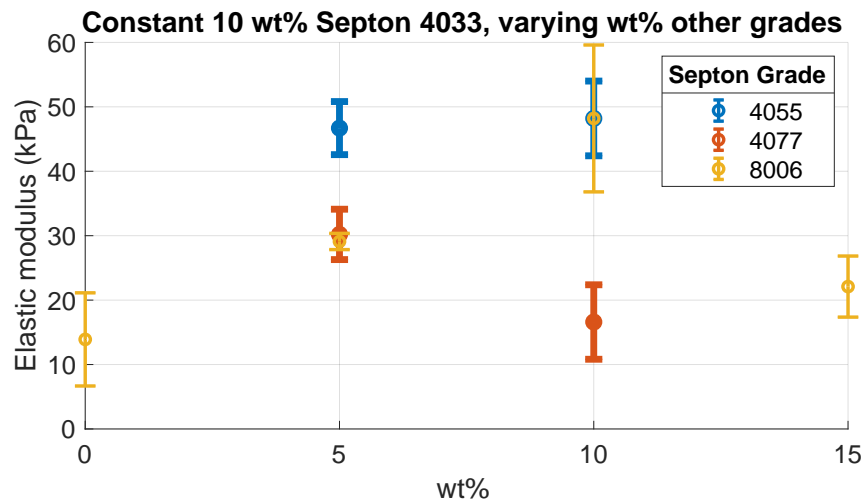


Figure 5.3: The changes in modulus observed as different grades of Septon are added to an oleogel formulation consisting of a constant weight percent of Septon 4033.

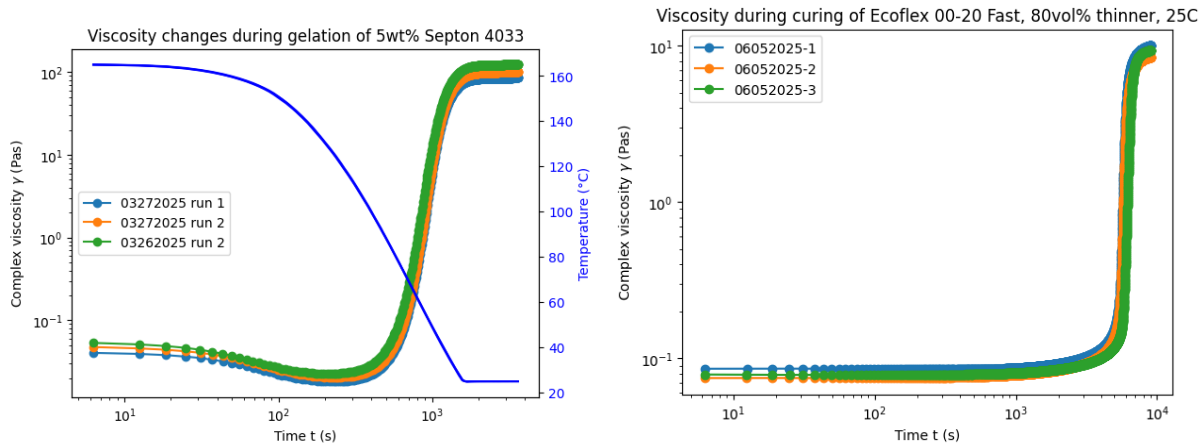


Figure 5.4: Comparisons of the complex viscosity γ of three samples of an oleogel formulation made up of 5wt% Septon 4033 and three samples of a silicone formulation made up of Ecoflex 00-20 FAST and 80vol% silicone thinner during gelation and curing, respectively.

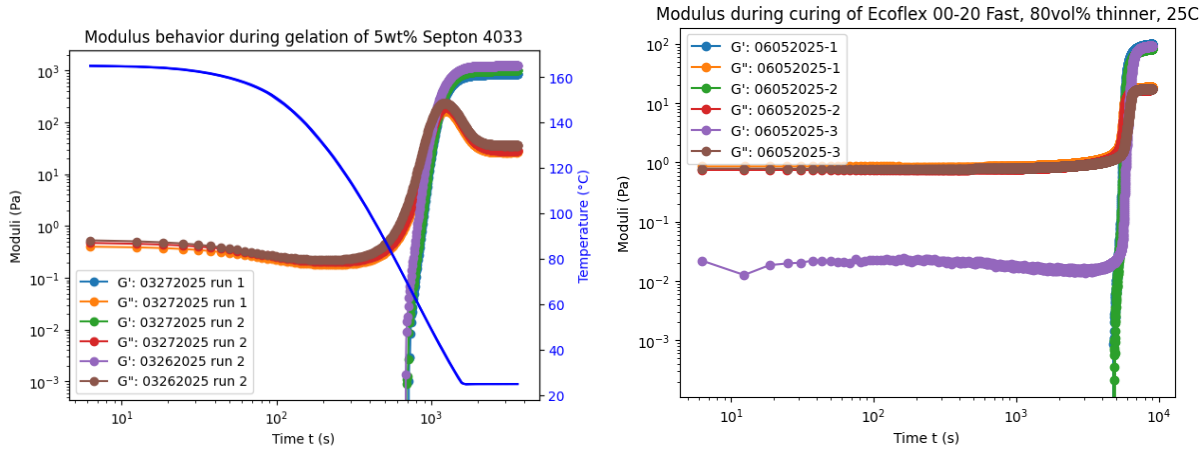


Figure 5.5: Comparisons of the shear storage and loss moduli (G' and G'') of three samples of an oleogel formulation made up of 5wt% Septon 4033 and three samples of a silicone formulation made up of Ecoflex 00-20 FAST and 80vol% silicone thinner during gelation and curing, respectively. In the right hand graph, the variation in initial G' between 06052025-3 and the other samples is likely due to the sample having begun to cure slightly earlier than the others.

In order to begin to control for these variables, we have determined the composition of a ‘matching silicone’ that is comparable to a chosen oleogel formulation (5% Septon 4033 by weight) in both initial complex viscosity γ and final shear storage modulus G' . To determine these baseline values for the oleogel, we determined a multi-part experimental protocol as follows:

1. **Sample preparation:** Prepare 5wt% Septon 4033 sample with 1 g Septon 4033, 19 g mineral oil for \approx 20 ml total volume in microcompounder, mixing for 15 minutes at 100 RPM, $250^{\circ}C$.
2. **Sample transport:** Extrude sample from microcompounder into small stainless steel container. Place container in thermos in order to inhibit cooling and gelation, and transport from fabrication area to rheometer lab.
3. **Rheological testing:** Pour sample into cup and bob rheometer attachment, which has already been heated to $165^{\circ}C$, and lower bob to test gap of 5925.6 microns. Make sure that no overflow occurs over the top of the bob. Run a time sweep at 5% strain limit while the cup and bob apparatus’ temperature drops back to $25^{\circ}C$, until the material has reached its terminal viscosity and modulus values.

The procedure for testing various types of Smooth-On brand silicone rubbers was similar, except that the silicones were all mixed by hand and the apparatus was not generally preheated. We chose silicones that the company datasheets indicated were comparatively low viscosity prior to curing and combined them with the Smooth-On brand silicone thinner. The varieties we tested included: Ecoflex Gel 2 Platinum, Ecoflex 00-20, Ecoflex 00-20 FAST, Ecoflex 00-45 Near Clear, Ecoflex Solaris, and Ecoflex Rubber Glass. Out of these, we found that the formulation with the most consistent/comparable complex viscosity and shear storage moduli values, as well as a comparable curing time, was Ecoflex 00-20 FAST with 80vol% silicone thinner.

Figures 5.4 and 5.5 show the results of the rheological testing described above. In Figure 5.4, we observe that the initial complex viscosity for the oleogel and silicone is slightly below 10^{-1} Pas (Pascal seconds). In Figure 5.5, we observe that the terminal shear moduli G' are about 1 kPa for the oleogel samples and 100 Pa for the silicone samples. If we do wish, however, to match the moduli, other tests show that this can be done by using Ecoflex 00-20 FAST with 30-50vol% silicone thinner, which still results in a fairly low initial viscosity as well (see Figure 5.6).

5.2 SEBS/SEEPS and Nd-Pr-Fe-B Composites

5.2.1 Deflection Testing

One of our material development interests lies in creating a material that deflects as much as possible given a fixed magnetic field. To that end, we designed the testing setup shown in Figure 5.7. In this setup, the flat, rectangular sample is secured between the resin-printed clamps and we measure the deflection distance and angle under electromagnetic attraction and repulsion using the Keyence TM-X5000 Telecentric Measurement System. The separation between the surface

Composition	Samples	Modulus (kPa)	Std. Dev.	Composition	Samples	Modulus (kPa)	Std. Dev.
15% 4033	7	35.9	3.98	10% 4033 5% 8006	3	29.1	1.26
10% 4033 5% 4077	3	30.2	3.91	15% 4033 5% 8006	3	64.1	14.8
15% 4033 5% 4077	3	77.3	2.74	5% 4033 10% 8006	3	8.02	2.72
5% 4033 10% 4077	0, failed	-	-	10% 4033 10% 8006	3	48.3	11.4
10% 4033 10% 4077	3	16.6	5.78	15% 4033 10% 8006	2	79.3	15.1
15% 4033 10% 4077	3	32.6	5.84	15% 8006	3	6.27	2.14
15% 4077	0, failed	-	-	5% 4033 15% 8006	2	22.5	3.80
5% 4033 15% 4077	2	7.76	3.49	10% 4033 15% 8006	3	22.1	4.74
10% 4033 15% 4077	1	29.9	-	15% 4033 15% 8006	2	118	21.6
15% 4033 15% 4077	0, failed	-	-	10% 4055 5% 4077	3	24.7	11.05
10% 4033 5% 4055	3	46.7	4.12	15% 4055 5% 4077	0, failed	-	-
15% 4033 5% 4055	3	80.5	0.127	5% 4055 10% 4077	3	12.4	7.29
5% 4033 10% 4055	3	29.71	21.94	10% 4055 10% 4077	0, failed	-	-
10% 4033 10% 4055	3	48.2	5.80	15% 4055 10% 4077	0, failed	-	-
15% 4033 10% 4055	3	69.7	4.52	5% 4055 15% 4077	0, failed	-	-
15% 4055	3	2.24	1.85	10% 4055 15% 4077	0, failed	-	-
5% 4033 15% 4055	3	9.88	2.87	10% 4055 5% 8006	3	23.1	10.6
10% 4033 15% 4055	0, failed	-	-	15% 4055 5% 8006	2	33.9	32.9
15% 4033 15% 4055	1	47.26	-	5% 4055 10% 8006	3	8.89	7.63

Table 5.2: Summary of results from SEBS/SEEPS combination sample fabrication and tensile testing, part I.

Composition	Samples	Modulus (kPa)	Std. Dev.	Composition	Samples	Modulus (kPa)	Std. Dev.
10% 4055	2	23.02	4.81	10% 8006	0, failed	-	-
10% 8006				5% 4033			
5% 4055	3	10.2	4.18	5% 8006	2	1.43	0.573
15% 8006				5% 4055			
10% 8006	2	7.90	5.09	5% 4077	0, failed	-	-
5% 4077				12.5% 8006			
15% 8006	0, failed	-	-	10% 4033	0, failed	-	-
5% 4077				15% 4033			
10% 8006	2	3.48	1.89	7.5% 4077	3	42.8	19.6
5% 4077				15% 4033	2	29.5	0.134
10% 8006	2	8.51	4.42	7.5% 4055			
10% 4077				12.5% 8006	1	19.4	-
15% 8006	2	8.88	1.01	10% 4033			
5% 4077				5% 8006	0, Failed	-	-
15% 4077	0, failed	-	-	5% 4077			
5% 8006	2	8.09	2.25				
15% 4077							
5% 4077	0, failed	-	-				
10% 4077	0, failed	-	-				
5% 4033	2	5.91	4.83				
5% 4033	0, failed	-	-				
5% 4077							
5% 4033	1	0.388	-				
10% 4077							
10% 4033	3	13.9	7.23				
5% 4055	0, failed	-	-				
10% 4055	0, failed	-	-				
5% 4033	3	1.78	0.934				
5% 4055							
5% 8006	0, failed	-	-				

Table 5.3: Summary of results from SEBS/SEEPS combination sample fabrication and tensile testing, part II.

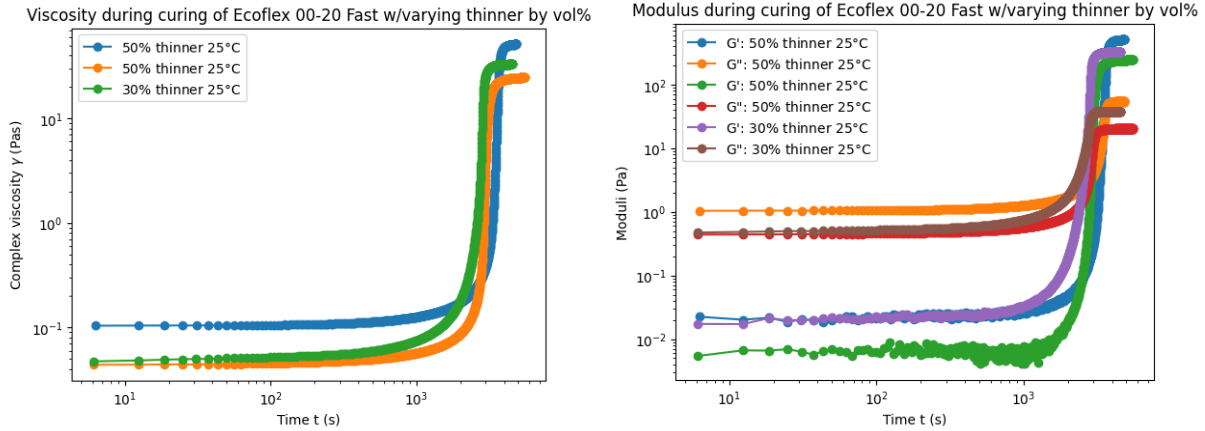


Figure 5.6: Viscosity and modulus behavior during curing for Ecoflex 00-20 FAST with 30-50 vol% silicone thinner. Terminal G' for this formulation is comparable to that of the tested oleogel.

of the sample and the tip of the electromagnet pole piece is set at 10 mm. As of present, we have tested 26 samples; the results of these experiments are summarized in Table 5.4. Out of this initial exploration, the most promising samples and results are as follows:

Greatest attraction distance (mm):

1. 9.71 mm: 6% 4055, 40% particles
2. 7.79 mm: 3% 4033, 2% 4077, 50% particles
3. 7.27 mm: 7% 4055, 30% particles

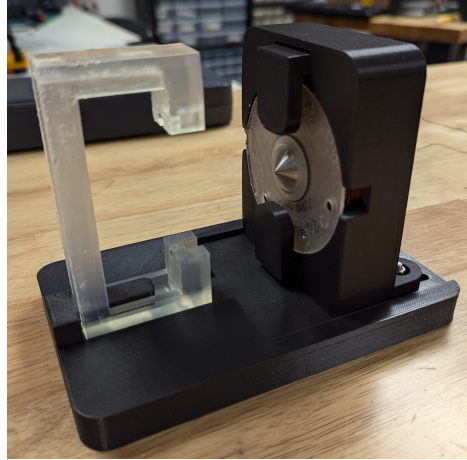
Greatest repulsion distance (mm):

1. 4.45 mm: 7% 4055, 30% particles
2. 3.95 mm: 3.5% 4055, 3.5% 8006, 30% particles
3. 3.27 mm: 6% 4055, 40% particles

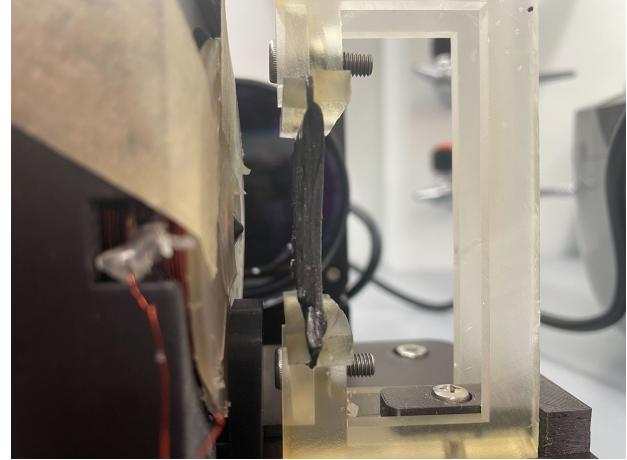
Greatest total deflection (repulsion plus attraction) distance (mm):

1. 12.98 mm: 6% 4055, 40% particles
2. 11.72 mm: 7% 4055, 30% particles
3. 10.36 mm: 3% 4033, 2% 4077, 50% particles

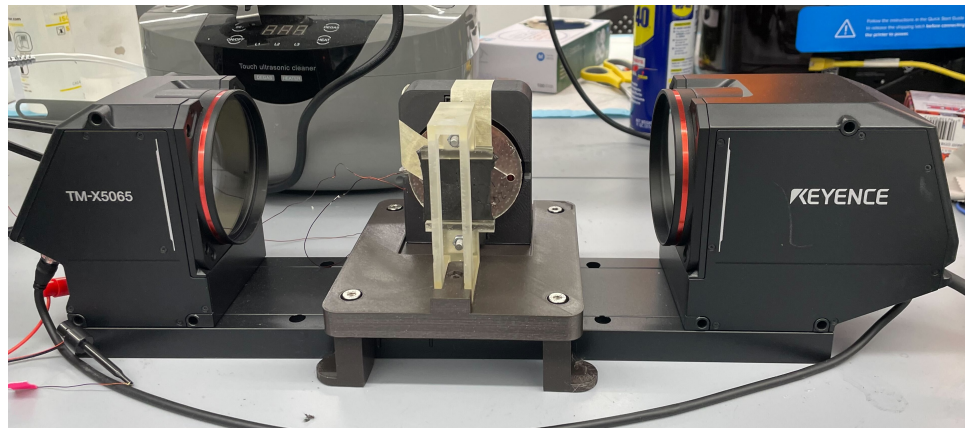
From our initial deflection testing, we have been able to show significant levels of deflection, with combined total deflection ranges > 10 mm. As expected, the deflection distance in the attraction direction exceeds the distance in the repulsion direction; this is likely due to the fact that the strength of the magnetic field is inversely proportional to the distance between the magnet and the sample, so as the sample is repulsed away from the magnet, the force on it decreases proportionally.



(a)



(b)



(c)

Figure 5.7: Custom electromagnetic deflection testing setup for magnetic material. **Top Left:** Partial testing setup with fixed electromagnet. **Top Right:** Detail of clamped sample prior to deflection. **Bottom:** Full testing setup including clamped sample, electromagnet, and TM-X5000 Optical Measurement System.

% Septon	Attract(mm)	Repulse(mm)	Att angle(°)	Rep angle(°)	% Particle
5.71% 4033	0.58	1.21	81.1	61.9	42.86
5.71% 4033	1.79	2.15	90	88.1	50.1
7% 4055	7.37	4.45	73	60.9	30
6% 4055	9.71	3.27	36.4	64.5	40
5% 4055	6.07	N/A	60.9	N/A	50
5% 4055	3.73	2.29	86.7	66.5	50
6% 4033	0.63	0.61	87	54.8	30
6% 4033	3.72	1.28	76.5	66.6	30
3.5% 8006 3.5% 4033	1.33	1.84	71.6	71.5	40
3.5% 8006 3.5% 4033	1.1	1.77	79.4	82	40
2.5% 8006 2.5% 4033	2.02	1.97	61.6	84.5	50
3% 4033 3% 4055	2.01	2.17	75.9	72.6	40
3% 4033 3% 4055	3.4	1.49	77.4	84.7	40
3% 4033 3% 4055	5.18	1.47	58.4	43.3	40
3.5% 4033 3.5% 4055	1.84	1.29	66.2	88.1	30
3.5% 4033 3.5% 4055	1.14	1.47	74.7	85.5	30
2.5% 4033 2.5% 4055	4.15	2.69	58.3	80.6	50
1% 4055 4% 4033	0.34	N/A	45	N/A	50
3% 4033 2% 4055	0.93	0.9	76.8	68.8	50
3% 4033 2% 4055	3.6	2.92	67.6	80.9	50
3% 4033 2% 4055	0.47	N/A	55.9	N/A	50
3% 4033, 2% 4077	7.79	2.57	34.8	78.3	50
3.5% 8006 3.5% 4055	5.36	3.95	73.8	81	30
3% 8006 3% 4055	6.02	1.2	65.8	74.7	40
3% 8006 3% 4055	3.9	2.01	75.5	61.3	40
3.5% 4077 3.5% 4055	2.32	N/A	60.1	N/A	30

Table 5.4: Summary of initial deflection results regarding distance traveled and angle of material under attraction and repulsion.

Due to fabrication irregularities, the samples tested were not all exactly comparable in terms of thickness, length, and width; certain issues with homogeneous particle distribution also emerged during processing. The dimensionality differences were largely due to the fact that the material often shrinks or contracts to varying degrees during gelation. An approach to normalize the sample dimensions would involve fabricating the samples in a mold larger than the desired dimensions and trimming the length and width to a standardized size (60mm × 50mm, resulting in a 50mm × 50mm area after clamping).

5.2.2 Modulus Testing

5.2.2.1 Modulus behavior during constant magnetic field exposure

In Section 5.1.2, we summarized our results regarding the behavior of a particular oleogel formulation as it goes through the process of gelation. Without any added magnetic particles, the shear storage modulus appears to reach a constant terminal value after the material cools to room temperature. In this vein, we wanted to try and quantify the oleogel behavior with added magnetic particles under an applied magnetic field. In order to do so, we conducted a series of tests using magnetic oleogel samples and an electromagnetic accessory for the DHR2 Rheometer. Each sample was composed of 5wt% Septon 4033, 45wt% mineral oil, and 50wt% neodymium alloy particles of the same type used in the previous chapters of this thesis. Each sample (unless otherwise noted) was prepared and transported similarly to the non-magnetic oleogel samples from Section 5.1.2. In each test, we continuously exposed the sample to a magnetic field $B = 300$ mT while under a 20 mm diameter parallel plate with a 1000 micron gap between plates. These experiments lasted between 30 minutes and 80 hours, depending on the sample. Figure 5.8 shows the results of several of these experiments, with sample details summarized below (note that data from samples 3a-c only appears in Section 5.2.2.2).

- Sample 1: 06232025-1 10ml sample, slightly cured before testing
- Sample 2: 06232025-2 20ml regular sample
- Sample 3: 07072025 first overnight sample
- Sample 3a: 07102025 rerun of 07072025 7 days after fabrication
- Sample 3b: 07112025 rerun of 07072025 8 days after fabrication
- Sample 3c: 07142025 rerun of 07072025 11 days after fabrication, 3 days of remagnetization
- Sample 7: 07182025-1 short cure time
- Sample 8: 07182025-2 long cure time
- Sample 9: 07212025 syringe reheat of excess 06232025-2

Despite our attempts to fabricate testable samples with identical formulations, the results of these tests showed high variability with respect to the behavior of G' . In the test of Sample 3, the initial storage modulus values were ≈ 2.5 times higher than the initial values for Samples 1 and

5wt% Septon 4033, 45wt% Mineral Oil, 50wt% NdFeB, Gelation under $B = 300$ mT

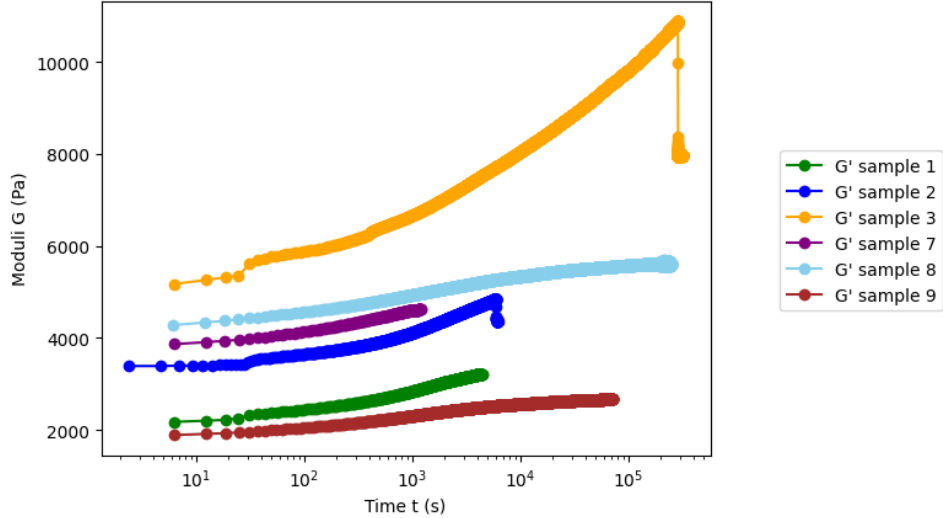


Figure 5.8: Shear storage modulus G' behavior over time for variously prepared samples of 5wt% Septon 4033, 45wt% mineral oil, and 50wt% NdFeB particles. The samples were all exposed to an applied magnetic field of $B = 300$ mT for the majority of each experiment - the drops in modulus observed for samples 2 and 3 occurred after the field returned to 0 mT.

9. It is also difficult to ascertain whether any of the samples have reached a plateau in terms of the modulus growth, and for Samples 2, 3, 7, and 8, the modulus appears to be actively increasing by the time the experiment is completed. While this growth is difficult to explain at this time, the behavior is not without precedent: experiments carried out in [4] using a SEBS-based oleogel with carbonyl iron particles show similar seemingly unbounded growth under the application of a 410 mT field for 600-800 seconds.

5.2.2.2 Dynamic modulus behavior

Since the most common use cases for magnetic soft materials are dynamic in nature (e.g. braking, gripping, varying a haptic sensation), we also wished to investigate the changes in the shear storage modulus under varying magnetic impulses. We were especially interested in the overall change in modulus from when the field is removed to when it is applied. To this end, we subjected several samples of 5wt% Septon 4033, 45wt% mineral oil, and 50wt% NdFeB particles to a repeated 10 seconds on, 10 seconds off 300 mT electromagnetic field under testing conditions identical to those described in Section 5.2.2.1. The results of these experiments are shown in Figure 5.9.

We observed some striking changes when we retested samples at different times. For example, samples 3, 3a, 3b, and 3c are actually the same physical sample tested at different times over the course of 11 days; when the sample is tested immediately after being gelated in a constant field for ≈ 80 hours (see Figure 5.8), the material shows a considerable jump in modulus from about 80 to 130 kPa when under the dynamically applied field. When the material is retested 7

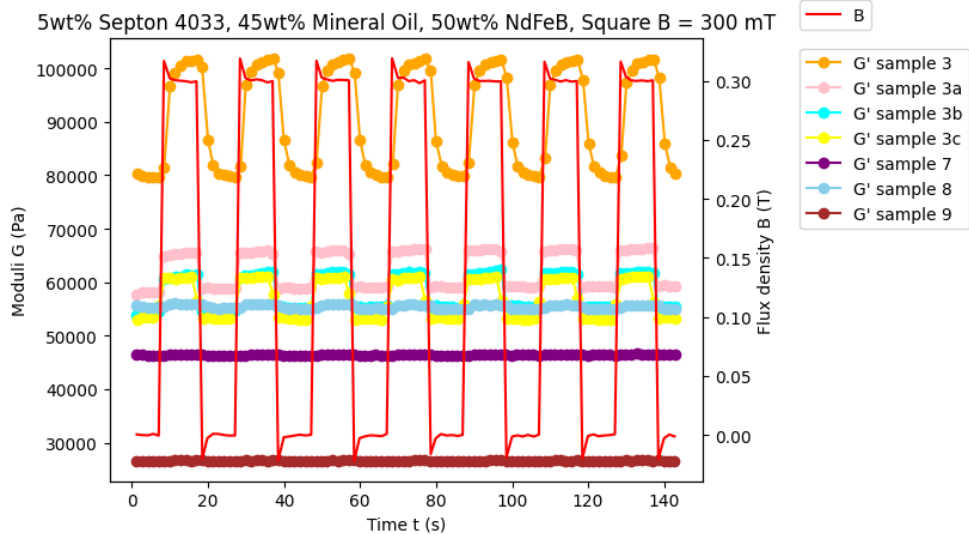


Figure 5.9: Impulse responses for variously prepared samples of 5wt% Septon 4033, 45wt% mineral oil, and 50wt% NdFeB particles with respect to a repeated 10 second step input of a 300 mT magnetic field.

and 8 days later (samples 3a and 3b, respectively), the baseline G' has dropped to below 60 kPa, and the change in modulus between the off and on inputs of the magnetic field is also diminished. Sample 3c shows an attempt to remagnetize the sample by leaving it on the surface of a permanent magnet generating a 300 mT field for 3 days, but the modulus behavior was nearly identical to what it had been prior to the remagnetization. In addition, samples 7-9 displayed only minor impulse responses when compared with the previous samples.

5.3 Conclusions

In this chapter, we have presented the results of a series of materials characterization experiments. We have put together a comprehensive set of reliable results regarding the varying tensile elastic moduli of different formulations of SEBS/SEEPS oleogels, which we have already used to select appropriate material formulations for a novel ultrasonic haptic device (Section 5.1.1). We have also determined the formulation of a suitable matching silicone for the use of creating and testing magnetic composites with similar characteristics to those made using oleogel bases (Section 5.1.2). In our experiments regarding magnetic oleogel composites, we have been able to determine several promising formulations for composites showing great deflection under an applied magnetic field, which could be of use in constructing soft grippers or shape-programmable interfaces (see Section 6.2 for further details). We also showed that oleogel-based magnetic composites are capable of notable static and dynamic behaviors under applied magnetic fields (Section 5.2.2), but that improvements in fabrication techniques will need to be developed in order to collect more consistent rheological data.

Chapter 6

Conclusion

6.1 Thesis Contributions

In this work, we show our progress towards the development fabrication and actuation methods for a highly deformable magnetic oleogel composite material that produces higher forces under magnetic actuation than more commonly used silicone composites. This material is composed of magnetic particles together with a low modulus elastomer, which are in turn processed together in a uniform magnetic field in order to induce a remanent magnetism in the material that allows it to be attracted or repulsed by a secondary field source after fabrication, e.g. one or more electromagnets. We have been able to show that samples made from oleogel and hard magnetic composites generate forces *an order of magnitude greater* than conventional silicone elastomers under equivalent driving conditions [19].

In the first part of this thesis, we introduced a magnetic wearable device that couples a low-modulus magnetic elastomer to a field-focusing electromagnet. In testing this device, we were able to show that *users perceive sensations directly proportional to the electromagnet input voltage* across both attraction and repulsion modalities. Building on this paradigm, we designed MAGTRACE (MAGnetic Texture Rendering for Active Contact and Exploration), a platform featuring dual electromagnets on a linear rail-mounted carriage that renders spatially varying shapes to the magnetic sheath on the user’s fingertip as they explore the shape environment by moving the carriage. Using this setup, we demonstrated that *users can reliably distinguish between virtual textures composed of sinusoidal, square, and sawtooth waveforms with varying spacings*, showing the potential of magnetic soft fingertip actuation in rendering complex haptic scenes.

The final part of this thesis concerns the mechanical characterization of the materials we have used in constructing the wearable components of these devices, namely SEBS/SEEPS triblock copolymer blends and the composites comprised of these materials and Nd-Pr-Fe-B particles. In this chapter, we were able to establish a formulation library to fabricate oleogels with desired values of tensile elastic moduli. We were also able to determine the formulation for a silicone with ‘matching’ characteristics with respect to a chosen oleogel formulation. Finally, we showed

a range of deflection and modulus behaviors for magnetic oleogel composites.

6.2 Future Work

6.2.1 Further Composite Materials Experiments

The final chapter of this thesis establishes several follow-on avenues for experimentation. Firstly, using the matching silicone material described in Section 5.1.2, we propose a set of experiments to compare the performance of composites made using the silicone and oleogel, respectively:

1. **Deflection testing:** using the experimental setup from Section 5.2.1, compare the deflection behavior of at least 3 samples each of 50wt% NdFeB composites made from 5wt% Septon 4033 and Ecoflex 00-20 FAST 80vol%.
2. **Force testing:** using the experimental setup from Section 3.2.2.3, compare the force output behavior of at least 3 samples each of 50wt% NdFeB composites made from 5wt% Septon 4033 and Ecoflex 00-20 FAST 80vol%.
3. **Remanent magnetism:** using a suitable magnetometer, compare the remanent magnetism of the deflection and force testing samples. Since magnetic force is directly related to the remanent magnetic field of a material, this may help explain any differences observed in force testing.

Since the matching material has been formulated to normalize across initial viscosity and terminal modulus values, it can be deduced that any differences in performance between composites made with the matched silicone and oleogel formulations are not due to those characteristics. If any differences arise, further investigation via microscopic material imaging will be necessary. We also propose the further study of the long-term behavior of magnetic oleogel composites. As seen in Section 5.2.2.2, leaving composite materials to sit for several days after initial magnetization can lead to notable changes in modulus responses to dynamically changing magnetic field inputs. Once suitable fabrication techniques have been developed for consistent rheological testing samples, further experiments regarding this phenomenon will help inform as to whether these composites are suitable for long-term use, and if they can possibly be “recharged” by reapplying an external magnetic field.

6.2.2 Magnetic Elastomers for Conformable Gripping Systems

Soft matter research can drive technology forward by developing safe, compliant materials for use in human-computer interaction and robotics. For robotics in particular, actuated elastomers could be used with robotic grippers to adaptively determine the shape and stiffness necessary to grasp delicate objects. While several research groups have introduced novel magnetic soft grippers, the mechanism by which they achieve grasping is generally to use changing magnetic fields to guide soft polymer appendages to open and close around a grasped object [80]. As an alternative to this form factor, we propose a design that leverages the high deformability of the materials developed in this work as a kind of augmentation to existing manipulator designs,

enabling the soft and compliant grasping of delicate or irregularly shaped objects as the gripper prongs approach each other.

The current state-of-the-art for compliant, soft gripping devices are those which use pneumatic particle jamming [10], which, while seemingly a promising modality, still has major limitations in terms of real-world viability. The resolution of the jamming surface is limited by the number of individual cells that can be controlled via individual pneumatic pumps, which can be difficult to coordinate due to latency in vacuum formation and release. Moreover, the reliance on pneumatic actuation limits the reliability of the device, since any surface puncture renders the affected cell inoperable, and the loud and bulky pumps detract from overall usability. An additional barrier to the deployment of soft actuators has to do with incorporating position or impedance sensing into the actuator for control purposes; while visuotactile sensors such as Gel-Sight have been able to provide new levels of information for gripping algorithms, they cannot do so while simultaneously acting as soft actuators, resulting in necessary tradeoffs at the location of the grasping interface [1].

Building on the contributions presented herein, we propose several novel directions in distinct research areas with the goal of improving the state-of-the-art in robotic manipulation. Firstly, we propose a novel gripping setup using an array of electromagnets that can be individually driven to actuate a magnetic elastomer that conforms around a gripped object. This gripping modality will improve on previous technology by leveraging its aforementioned advantages for improved resolution and reliability, as well as by using the built-in benefits of magnetic actuation. For example, using the ability of the material to be quickly repulsed by an electromagnet, the proposed gripper would be able to immediately let go of an object without having to wait for the rearrangement of particles (as in particle jamming).

Secondly, we propose the incorporation of recent advances in magnetometer-based remanent field sensing [8, 29, 30] to develop a novel concomitant sensing method in soft actuators. The principle behind magnetic soft sensing is that upon deformation, the remanent fields in a magnetized soft material will vary in proportion to the deforming force, and the variations can be measured and interpreted using small-scale magnetometers near the material. These sensors have been shown to detect forces from 0.1 - 2.5N, which is sufficient to handle the force exerted by a \approx 1-pound object in a robot gripper. In order to implement feedback control of a magnetic gripper, one could use a similar field-sensing approach to interpret the forces applied to a magnetic soft material, which could then be fed into a control loop that would allow the system to adjust current directions and magnitudes to the electromagnets in order to maintain the optimal shape for grasping a particular object.

6.2.3 Shape-Programmable Interfaces

Shape-programmable interfaces (SPIs), which are deformable surfaces that can be driven to change shape, have the potential to be used to deliver touchable information in a virtual reality or teleoperation setting. Based on the research presented here, we propose building an SPI

using an array of electromagnets that can be individually driven to controllably deform a sheet of magnetic elastomer in order to form desired shapes for haptic displays and for use as an end effector on a robot arm in grasping fragile objects. Given the limitations in current technology based on pneumatic actuation, e.g. jamming surfaces such [69], this SPI would have the potential have higher resolution and reliability than existing devices.

To model and control such SPIs, we propose using a subset of the primitives discussed in [81] (namely stretching, source, and 2D bending) to develop a primitive-based kinematic model for SPI shape formation. Since the actuation of a magnetic soft material is dependent on magnitude and direction of the applied magnetic field, it can be considered the “input” parameter to control the material shape. Using the kinematic model, its Jacobian can be used to derive the inputs that will drive the material to a desired shape. This method is more computationally efficient than traditional ways of modeling soft materials, such as finite element analysis [81], allowing for more effective incorporation into a control loop. To implement feedback control of an SPI-based haptic display, one could use a field-sensing approach similar to those presented in [8, 29, 30] to interpret the forces applied to a magnetic soft SPI, which would then be fed into a control loop that would allow the SPI system to adjust current directions and magnitudes to the electromagnets in order to maintain a desired shape.

Bibliography

- [1] Alexander C Abad and Anuradha Ranasinghe. Visuotactile sensors with emphasis on gel-sight sensor: A review. *IEEE Sensors Journal*, 20(14):7628–7638, 2020. 6.2.2
- [2] Moaed A. Abd, Joseph Ingicco, Douglas T. Hutchinson, Emmanuelle Tognoli, and Erik D. Engeberg. Multichannel haptic feedback unlocks prosthetic hand dexterity. *Scientific Reports*, 12(1), 2022. 3.2.2.1
- [3] Mine Begum Alanalp and Ali Durmus. Quantifying microstructural, thermal, mechanical and solid-state viscoelastic properties of polyolefin blend type thermoplastic elastomer compounds. *Polymer*, 142:267–276, 2018. 5
- [4] Hai-Ning An, Bin Sun, Stephen J Picken, and Eduardo Mendes. Long time response of soft magnetorheological gels. *The Journal of Physical Chemistry B*, 116(15):4702–4711, 2012. 5.2.2.1
- [5] American Psychological Association. *APA Dictionary of Psychology*. American Psychological Association, 2015. 4.3.3.2
- [6] Konstantinos B. Baltzis. The femm package: A simple, fast, and accurate open source electromagnetic tool in science and engineering. *Journal of Engineering Science & Technology Review*, 1(1), 2008. 3.2.1
- [7] Cagatay Basdogan, Frederic Giraud, Vincent Levesque, and Seungmoon Choi. A review of surface haptics: Enabling tactile effects on touch surfaces. *IEEE transactions on haptics*, 13(3):450–470, 2020. 2.1
- [8] Raunaq Bhirangi, Tess Hellebrekers, Carmel Majidi, and Abhinav Gupta. Reskin: versatile, replaceable, lasting tactile skins. *arXiv preprint arXiv:2111.00071*, 2021. 6.2.2, 6.2.3
- [9] Shantonu Biswas and Yon Visell. Haptic perception, mechanics, and material technologies for virtual reality. *Advanced Functional Materials*, 31(39):2008186, 2021. 2.1
- [10] Eric Brown, Nicholas Rodenberg, John Amend, Annan Mozeika, Erik Steltz, Mitchell R. Zakin, Hod Lipson, and Heinrich M. Jaeger. Universal robotic gripper based on the jamming of granular material. *Proceedings of the National Academy of Sciences*, 107(44):18809–18814, October 2010. ISSN 1091-6490. doi: 10.1073/pnas.1003250107. URL <http://dx.doi.org/10.1073/pnas.1003250107>. 6.2.2
- [11] David A Burns, Roberta L Klatzky, Michael A Peshkin, and J Edward Colgate. The single-pitch texel: A flexible and practical texture-rendering algorithm. *PNAS nexus*, 3(1):452, 2024. 2.1, 4.2.4

- [12] David Arthur Burns, Roberta L Klatzky, Michael A Peshkin, and J Edward Colgate. A low-parameter rendering algorithm for fine textures. *IEEE transactions on haptics*, 15(1):57–61, 2021. 2.1
- [13] Manuel Caeiro-Rodríguez, Iván Otero-González, Fernando A Mikic-Fonte, and Martín Llamas-Nistal. A systematic review of commercial smart gloves: Current status and applications. *Sensors*, 21(8):2667, 2021. 2.1
- [14] Gianni Campion and Vincent Hayward. Fundamental limits in the rendering of virtual haptic textures. In *First Joint Eurohaptics Conference and Symposium on Haptic Interfaces for Virtual Environment and Teleoperator Systems. World Haptics Conference*, pages 263–270. IEEE, 2005. 2.1
- [15] Ludovico Cestarollo, Shane Smolenski, and Amal El-Ghazaly. Nanoparticle-based magnetorheological elastomers with enhanced mechanical deflection for haptic displays. *ACS Applied Materials & Interfaces*, 14(16):19002–19011, 2022. 2.2
- [16] John Y. Chen. Gelatinous elastomer articles, May 27 1997. US Patent 5,633,286. 3.2.2.1
- [17] Dong-Soo Choi, Tae-Hoon Kim, Seok-Han Lee, Changhyun Pang, Jin Woo Bae, and Sang-Youn Kim. Beyond human hand: shape-adaptive and reversible magnetorheological elastomer-based robot gripper skin. *ACS Applied Materials & Interfaces*, 12(39):44147–44155, 2020. 2.2
- [18] Seungmoon Choi and Hong Z Tan. Toward realistic haptic rendering of surface textures. In *ACM SIGGRAPH 2005 Courses*, pages 125–es. 2005. 2.1
- [19] Sarah Costrell, Mahirah Alam, Roberta L. Klatzky, Michael E. McHenry, Lynn M. Walker, and Melisa Orta Martinez. A magnetic soft device for tactile haptic actuation of the fingertip. In *2023 IEEE World Haptics Conference (WHC)*, pages 48–55. IEEE, 2023. 6.1
- [20] Heather Culbertson, Juan José López Delgado, and Katherine J Kuchenbecker. One hundred data-driven haptic texture models and open-source methods for rendering on 3d objects. In *2014 IEEE haptics symposium (HAPTICS)*, pages 319–325. IEEE, 2014. 2.1
- [21] Heather Culbertson, Samuel B. Schorr, and Allison M. Okamura. Haptics: The present and future of artificial touch sensation. *Annual Review of Control, Robotics, and Autonomous Systems*, 1(1):385–409, 2018. 1, 2.1
- [22] Wang Dangxiao, Guo Yuan, Liu Shiyi, Yuru Zhang, Xu Weiliang, and Xiao Jing. Haptic display for virtual reality: progress and challenges. *Virtual Reality & Intelligent Hardware*, 1(2):136–162, 2019. 2.1
- [23] Ali Durmus, Mine Begum Alanalp, and Ismail Aydin. Investigation of rheological behaviors of polyolefin blend type thermoplastic elastomers for quantifying microstructure-property relationships. *Korea-Australia Rheology Journal*, 31:97–110, 2019. 5
- [24] James Alfred Ewing. *Magnetic induction in iron and other metals*. D. Van Nostrand Company, 1900. 3.2.1
- [25] Jason P Fritz and Kenneth E Barner. Stochastic models for haptic texture. In *Telemanipulator and Telepresence Technologies III*, volume 2901, pages 34–44. SPIE, 1996. 2.1
- [26] Wei Gao, Lanlan Wang, Xingzhe Wang, and Hongzhong Liu. Magnetic driving flowerlike

- soft platform: Biomimetic fabrication and external regulation. *ACS Applied Materials & Interfaces*, 8(22):14182–14189, 2016. 2.2
- [27] Roman V Grigorii, Roberta L Klatzky, and J Edward Colgate. Data-driven playback of natural tactile texture via broadband friction modulation. *IEEE Transactions on Haptics*, 15(2):429–440, 2021. 2.1
- [28] Jianglong Guo, Jinsong Leng, and Jonathan Rossiter. Electroadhesion technologies for robotics: A comprehensive review. *IEEE Transactions on Robotics*, 36(2):313–327, 2019. 2.1
- [29] Tess Hellebrekers, Oliver Kroemer, and Carmel Majidi. Soft magnetic skin for continuous deformation sensing. *Advanced Intelligent Systems*, 1(4):1900025, 2019. 6.2.2, 6.2.3
- [30] Tess Hellebrekers, Nadine Chang, Keene Chin, Michael J Ford, Oliver Kroemer, and Carmel Majidi. Soft magnetic tactile skin for continuous force and location estimation using neural networks. *IEEE Robotics and Automation Letters*, 5(3):3892–3898, 2020. 6.2.2, 6.2.3
- [31] Negin Heravi, Heather Culbertson, Allison M Okamura, and Jeannette Bohg. Development and evaluation of a learning-based model for real-time haptic texture rendering. *IEEE Transactions on Haptics*, 2024. 2.1
- [32] Mark Hollins and S Ryan Risner. Evidence for the duplex theory of tactile texture perception. *Perception & psychophysics*, 62(4):695–705, 2000. 4
- [33] Ya Huang, Kuanming Yao, Jiyu Li, Dengfeng Li, Huiling Jia, Yiming Liu, Chun Ki Yiu, Wooyoung Park, and Xinge Yu. Recent advances in multi-mode haptic feedback technologies towards wearable interfaces. *Materials Today Physics*, 2021. 1
- [34] Yoshikazu Ishikawa and Sōshin Chikazumi. Design of high power electromagnets. *Japanese Journal of Applied Physics*, 1(3):155–173, 1962. 3.2.1, 4.2.2
- [35] Yvonne Jansen. Mudpad: fluid haptics for multitouch surfaces. In *CHI’10 Extended Abstracts on Human Factors in Computing Systems*, pages 4351–4356. 2010. 2.2
- [36] William H Jantscher, Shivam Pandey, Priyanshu Agarwal, Sadie H Richardson, Bowie R Lin, Michael D Byrne, and Marcia K O’Malley. Toward improved surgical training: Delivering smoothness feedback using haptic cues. In *2018 IEEE haptics symposium (HAPTICS)*, pages 241–246. IEEE, 2018. 2.1
- [37] David Katz and Lester E Krueger. *The world of touch*. Psychology press, 2013. 4
- [38] H. Hawkeye King, Regina Donlin, and Blake Hannaford. Perceptual thresholds for single vs. multi-finger haptic interaction. In *2010 IEEE Haptics Symposium*, pages 95–99. IEEE, 2010. 3.1
- [39] Laure K. Lagorce, Oliver Brand, and Mark G. Allen. Magnetic microactuators based on polymer magnets. *Journal of Microelectromechanical Systems*, 8(1):2–9, 1999. 2.2
- [40] Susan J Lederman and Roberta L Klatzky. Hand movements: A window into haptic object recognition. *Cognitive psychology*, 19(3):342–368, 1987. 4
- [41] Jack M Loomis. Distal attribution and presence. *Presence: Teleoperators and virtual*

environments, 1(1):113–119, 1992. 4

- [42] Xiushou Lu, Xiuying Qiao, Hiroshi Watanabe, Xinglong Gong, Tao Yang, Wei Li, Kang Sun, Meng Li, Kang Yang, Hongen Xie, et al. Mechanical and structural investigation of isotropic and anisotropic thermoplastic magnetorheological elastomer composites based on poly (styrene-b-ethylene-co-butylene-b-styrene)(sebs). *Rheologica acta*, 51(1):37–50, 2012. 5
- [43] Luc Marechal, Pascale Balland, Lukas Lindenroth, Fotis Petrou, Christos Kontovounisios, and Fernando Bello. Toward a common framework and database of materials for soft robotics. *Soft Robotics*, 8(3):284–297, 2021. (document), 3.1
- [44] Alex Mazursky, Shan-Yuan Teng, Romain Nith, and Pedro Lopes. Magnetio: Passive yet interactive soft haptic patches anywhere. In *Proceedings of the 2021 CHI Conference on Human Factors in Computing Systems*, pages 1–15, 2021. 2.2
- [45] Michael E. McHenry, R. Swaminathan, K. J. Miller, A. H. Habib, N. J. Jones, and K. L. McNerny. The role of surface crystallography, faceting and chaining in magnetic applications of nanoparticles and nanocomposites. *NEPTIS: Nissrin Engineering Particle Technology International Seminar*, 18:5–14, 2009. 2.2
- [46] Jess McIntosh, Paul Strohmeier, Jarrod Knibbe, Sebastian Boring, and Kasper Hornbæk. Magnetips: Combining fingertip tracking and haptic feedback for around-device interaction. In *Proceedings of the 2019 CHI Conference on Human Factors in Computing Systems*, pages 1–12, 2019. 2.2
- [47] David J Meyer, Michael A Peshkin, and J Edward Colgate. Fingertip friction modulation due to electrostatic attraction. In *2013 world haptics conference (WHC)*, pages 43–48. IEEE, 2013. 2.1
- [48] David J Meyer, Michael A Peshkin, and J Edward Colgate. Tactile paintbrush: A procedural method for generating spatial haptic texture. In *2016 IEEE Haptics Symposium (HAPTICS)*, pages 259–264. IEEE, 2016. 2.1
- [49] Joe Mullenbach, Craig Shultz, J Edward Colgate, and Anne Marie Piper. Exploring affective communication through variable-friction surface haptics. In *Proceedings of the SIGCHI Conference on Human Factors in Computing Systems*, pages 3963–3972, 2014. 2.1
- [50] Thomas Mulvey. Unconventional lens design. In *Magnetic electron lenses*, pages 359–412. Springer, 1982. 3.2.1
- [51] Anne M. Murray, Roberta L. Klatzky, and Pradeep K. Khosla. Psychophysical characterization and testbed validation of a wearable vibrotactile glove for telemanipulation. *Presence: Teleoperators & Virtual Environments*, 12(2):156–182, 2003. 3.3.2, 3.3.3
- [52] Jun Nishida, Daisuke Tajima, Yasuko Namikawa, and Shunichi Kasahara. Demonstrating magnus: A magnetic hand exoskeleton for fast and dexterous finger actuation. In *ACM SIGGRAPH 2024 Emerging Technologies*, pages 1–2. 2024. 2.2
- [53] Akihiro Nishioka, Yuji Aoki, Takaya Suzuki, Akira Ishigami, Tomohiro Endo, Tomonori Koda, and Kiyohito Koyama. Dynamic mechanical properties of polystyrene-block-poly [ethylene-co-(ethylene-propylene)]-block-polystyrene triblock copolymer/hydrocarbon oil

blends. *Journal of Applied Polymer Science*, 121(5):3001–3006, 2011. 5

- [54] Claudio Pacchierotti, Stephen Sinclair, Massimiliano Solazzi, Antonio Frisoli, Vincent Hayward, and Domenico Prattichizzo. Wearable haptic systems for the fingertip and the hand: taxonomy, review, and perspectives. *IEEE Transactions on Haptics*, 10(4):580–600, 2017. 1, 2.1, 4.1
- [55] Michel Paré, Heather Carnahan, and Allan M. Smith. Magnitude estimation of tangential force applied to the fingerpad. *Experimental Brain Research*, 142:342–348, 2002. 3.3.3
- [56] Tony M Pearce. Gelatinous elastomer and methods of making and using the same and articles made therefrom, November 30 1999. US Patent 5,994,450. 4.2.1
- [57] Song Qi, Hengyu Guo, Jie Fu, Yuanpeng Xie, Mi Zhu, and Miao Yu. 3d printed shape-programmable magneto-active soft matter for biomimetic applications. *Composites Science and Technology*, 188, 2020. 2.2
- [58] Xiuying Qiao, Xiushou Lu, Weihua Li, Jun Chen, Xinglong Gong, Tao Yang, Wei Li, Kang Sun, and Xiaodong Chen. Microstructure and magnetorheological properties of the thermoplastic magnetorheological elastomer composites containing modified carbonyl iron particles and poly (styrene-b-ethylene-ethylenepropylene-b-styrene) matrix. *Smart Materials and Structures*, 21(11):115028, 2012. 5
- [59] Xiuying Qiao, Xiushou Lu, Xinglong Gong, Tao Yang, Kang Sun, and Xiaodong Chen. Effect of carbonyl iron concentration and processing conditions on the structure and properties of the thermoplastic magnetorheological elastomer composites based on poly (styrene-b-ethylene-co-butylene-b-styrene)(sebs). *Polymer Testing*, 47:51–58, 2015. 5
- [60] Yosra Rekik, Eric Vezzoli, Laurent Grisoni, and Frédéric Giraud. Localized haptic texture: A rendering technique based on taxels for high density tactile feedback. In *Proceedings of the 2017 CHI Conference on Human Factors in Computing Systems*, pages 5006–5015, 2017. 2.1
- [61] Ziyu Ren, Wenqi Hu, Xiaoguang Dong, and Metin Sitti. Multi-functional soft-bodied jellyfish-like swimming. *Nature Communications*, 10(1):1–12, 2019. 2.2
- [62] Ronald E. Rosensweig. On magnetorheology and electrorheology as states of unsymmetric stress. *Journal of Rheology*, 39(1):179–192, 1995. 2.2
- [63] Jace Rozsa, Sarah Costrell, Melisa Orta Martinez, and Gary K Fedder. Fingertip ultrasonic array for tactile rendering. In *2024 IEEE International Conference on Robotics and Automation (ICRA)*, pages 9682–9688. IEEE, 2024. 2.1, 5.1.1
- [64] Muzalifah Mohd Said, Jumril Yunas, Roer Eka Pawinanto, Burhanuddin Yeop Majlis, and Badariah Bais. Pdms based electromagnetic actuator membrane with embedded magnetic particles in polymer composite. *Sensors and Actuators A: Physical*, 245:85–96, 2016. 2.2
- [65] Kenneth Salisbury, Francois Conti, and Federico Barbagli. Haptic rendering: introductory concepts. *IEEE computer graphics and applications*, 24(2):24–32, 2004. 2.1
- [66] Enzo Pasquale Scilingo, Nicola Sgambelluri, Danilo De Rossi, and Antonio Bicchi. Haptic displays based on magnetorheological fluids: design, realization and psychophysical validation. In *11th Symposium on Haptic Interfaces for Virtual Environment and Teleoperator*

Systems, 2003. HAPTICS 2003. Proceedings., pages 10–15. IEEE, 2003. 2.2

- [67] Claudia Simonelli, Antonino Musolino, Rocco Rizzo, and Lynette A. Jones. Development of an innovative magnetorheological fluids-based haptic device excited by permanent magnets. In *2021 IEEE World Haptics Conference (WHC)*, pages 61–66. IEEE, 2021. 2.2
- [68] Oliver Snyder, Rebeka Almasi, Cathy Fang, Roberta L Klatzky, and George Stetten. Assessment of surface rendering with 1 dof vibration. *Computer Methods in Biomechanics and Biomedical Engineering: Imaging & Visualization*, 9(4):400–406, 2021. 4
- [69] Andrew A Stanley, Kenji Hata, and Allison M Okamura. Closed-loop shape control of a haptic jamming deformable surface. In *2016 IEEE International Conference on Robotics and Automation (ICRA)*, pages 2718–2724. IEEE, 2016. 6.2.3
- [70] Zhongda Sun, Minglu Zhu, Xuechuan Shan, and Chengkuo Lee. Augmented tactile-perception and haptic-feedback rings as human-machine interfaces aiming for immersive interactions. *Nature Communications*, 13(1), 2022. 3.2.2.1
- [71] Aishwari Talhan, Hwangil Kim, and Seokhee Jeon. Tactile ring: Multi-mode finger-worn soft actuator for rich haptic feedback. *IEEE Access*, 8:957–966, 2019. 3.2.2.1
- [72] Sylvia Tan, R. Daelan Roosa, Roberta L. Klatzky, Michael A. Peshkin, and J. Edward Colgate. A soft wearable tactile device using lateral skin stretch. In *2021 IEEE World Haptics Conference (WHC)*, pages 697–702. IEEE, 2021. 2.2
- [73] Justina Vaicekauskaite, Piotr Mazurek, Sindhu Vudayagiri, and Anne Ladegaard Skov. Mapping the mechanical and electrical properties of commercial silicone elastomer formulations for stretchable transducers. *Journal of Materials Chemistry C*, 8(4):1273–1279, 2020. 3.2.2.1
- [74] Venkatasubramanian Kalpathy Venkiteswaran, Danica Kristina Tan, and Sarthak Misra. Tandem actuation of legged locomotion and grasping manipulation in soft robots using magnetic fields. *Extreme Mechanics Letters*, 41, 2020. 2.2
- [75] Hongman Wang, Zhisen Zhu, He Jin, Rui Wei, Lei Bi, and Wenling Zhang. Magnetic soft robots: Design, actuation, and function. *Journal of Alloys and Compounds*, 2022. 3.2.2.1
- [76] Zhixin Wang, Alex A. Volinsky, and Nathan D. Gallant. Crosslinking effect on poly-dimethylsiloxane elastic modulus measured by custom-built compression instrument. *Journal of Applied Polymer Science*, 131(22), 2014. 3.2.2.1
- [77] Malte Weiss, Chat Wacharamanotham, Simon Voelker, and Jan Borchers. Fingerflux: near-surface haptic feedback on tabletops. In *Proceedings of the 24th Annual ACM Symposium on User Interface Software and Technology*, pages 615–620, 2011. 2.2
- [78] Laura Winfield, John Glassmire, J Edward Colgate, and Michael Peshkin. T-pad: Tactile pattern display through variable friction reduction. In *Second Joint EuroHaptics Conference and Symposium on Haptic Interfaces for Virtual Environment and Teleoperator Systems (WHC'07)*, pages 421–426. IEEE, 2007. 2.1
- [79] Shuai Wu, Wenqi Hu, Qiji Ze, Metin Sitti, and Ruike Zhao. Multifunctional magnetic soft composites: A review. *Multifunctional Materials*, 3(4), 2020. 3.2.2.1
- [80] Meng Xu, Yang Liu, Jialei Li, Fu Xu, Xuefeng Huang, and Xiaobin Yue. Review of flexible

robotic grippers, with a focus on grippers based on magnetorheological materials. *Materials*, 17(19):4858, 2024. 6.2.2

- [81] Yi Xu and Gregory S Chirikjian. Model reduction in soft robotics using locally volume-preserving primitives. *IEEE Robotics and Automation Letters*, 8(9):5831–5838, 2023. 6.2.3
- [82] Warren C. Young and Richard G. Budynas. *Roark's formulas for stress and strain: Warren C. Young; Richard G. Budynas*. McGraw-Hill, 2002. 3.2.2.1
- [83] Qiji Ze, Xiao Kuang, Shuai Wu, Janet Wong, S. Macrae Montgomery, Rundong Zhang, Joshua M. Kovitz, Fengyuan Yang, H. Jerry Qi, and Ruike Zhao. Magnetic shape memory polymers with integrated multifunctional shape manipulation. *Advanced Materials*, 32(4), 2020. 2.2
- [84] Zheng Zhang, Xianghao Li, Xiaochen Yu, Hao Chai, Yang Li, Huaping Wu, and Shaofei Jiang. Magnetic actuation bionic robotic gripper with bistable morphing structure. *Composite Structures*, 229, 2019. 2.2
- [85] Huichan Zhao, Aftab M. Hussain, Ali Israr, Daniel M. Vogt, Mihai Duduta, David R. Clarke, and Robert J. Wood. A wearable soft haptic communicator based on dielectric elastomer actuators. *Soft Robotics*, 7(4):451–461, 2020. 3.2.2.1
- [86] Mengjia Zhu, Shantonu Biswas, Stejara Iulia Dinulescu, Nikolas Kastor, Elliot Wright Hawkes, and Yon Visell. Soft, wearable robotics and haptics: Technologies, trends, and emerging applications. *Proceedings of the IEEE*, 110(2):246–272, 2022. 2.2
- [87] Minglu Zhu, Zhongda Sun, Zixuan Zhang, Qiongfeng Shi, Tianyi He, Huicong Liu, Tao Chen, and Chengkuo Lee. Haptic-feedback smart glove as a creative human-machine interface (hmi) for virtual/augmented reality applications. *Science Advances*, 6(19), 2020. 3.2.2.1
- [88] Jozef J. Zwislocki and D.A. Goodman. Absolute scaling of sensory magnitudes: A validation. *Perception & Psychophysics*, 28(1):28–38, 1980. 3.3.2